Synthesis of launch vehicle design and trajectory optimization

by

Veena Savithri Dorairajan

A Thesis Submitted to the

Graduate Faculty in Partial Fulfillment of the

Requirements for the Degree of

MASTER OF SCIENCE

Department: Aerospace Engineering and Engineering Mechanics
Major: Aerospace Engineering

Iowa State University
Ames, Iowa
1995

TABLE OF CONTENTS

LIST OF TABLES

LIST OF FIGURES

NOMENCLATURE

C_d	drag coefficient;
C_f	total skin-friction coefficient of the vehicle;
C_{fL}	skin-friction coefficient for laminar flow;
C_{fT}	skin-friction coefficient for turbulent flow;
C_L	lift coefficient;
C_N	normal-force coefficient;
$C_{N\alpha}$	aerodynamic normal-force-curve slope (variation of C_N with α);
D	drag force, *lbs*;
I_{sp}	specific impulse, *sec*;
J	performance index;
K	propellant sensitive mass fraction;
L	lift force, *lbs*;
M	Mach number;
Re	Reynolds number;
S	reference area of vehicle, ft^2;
S_L	wetted area over length l, ft^2;
S_X	wetted area over length l_{cone}, ft^2;
T	Thrust, *lbs*;

$a(h)$	speed of sound at altitude h, $\frac{ft}{sec}$;
$\frac{d}{l}$	slenderness ratio;
d	diameter of vehicle, ft;
g	acceleration due to gravity, $\frac{ft}{sec^2}$;
g_s	acceleration due to gravity on earth's surface, $\frac{ft}{sec^2}$;
h	altitude, ft;
l	vehicle length, ft;
l_{cone}	nose-cone length, ft;
m	vehicle instantaneous mass, $slugs$;
m_0	initial mass, $slugs$;
m_{stru}	stage structural mass, $slugs$;
m_{cone}	structural mass of cone-cylinder that houses the payload, $slugs$;
m_{prop}	stage propellant mass, $slugs$;
m_{PL}	payload mass, $slugs$;
s	surface range, ft;
t_1	first-stage burn time, sec;
t_2	second-stage burn-out time, sec;
v	vehicle velocity, $\frac{ft}{sec}$;
α	angle-of-attack, rad;
β	propellant mass flow rate, $slug/sec$;
δ	thrust steering angle, rad;
γ	flight-path-angle, rad;
μ	viscosity of air, $\frac{slug}{ft-sec}$;
ν	kinematic viscosity of air, $\frac{ft^2}{sec}$;

ρ	density of air, $\frac{slug}{ft^3}$;
σ	nosecone half-angle, deg;
τ	normalized time, $\tau = \frac{t}{t_f}$;
θ	pitch angle, rad;

ACKNOWLEDGMENTS

I am deeply indebted to my major professor Dr. Bion Pierson, for his invaluable guidance and advise in my research and graduate studies. Special thanks go to Dr. Jerry Vogel for his time and wisdom in sorting out some design problems I faced in course of my research. Most importantly, I would like to thank my husband Sugumar and my parents for their patience and encouragement.

CHAPTER 1. INTRODUCTION

Motivation and historical background

For years, launch vehicle designers and control personnel have worked in isolation without much interaction in designing the vehicle. Usually, the design group hands over a frozen vehicle configuration to the trajectory and controls group to find the optimal trajectory and best control design possible for that particular configuration. The purpose of this research is to show the advantages of combined trajectory and vehicle design optimization. This combination stresses the importance of controls personnel participating in vehicle design at a much earlier stage.

Maximizing payload capability of a multistage launch vehicle flown to a prescribed set of burnout conditions is a problem that frequently arises in trajectory optimization studies. If all the vehicle parameters are specified, the problem reduces to that of finding the optimum steering profile. In many cases, however, not all these parameters are specified, and those left unspecified can be varied to maximize payload. A typical situation that occurs in the design of future launch vehicles is one in which the propulsion system (thrust and propellant flow rate) is specified, but some or all the propellant loading are left unspecified. The unspecified propellant loadings generally can be varied to achieve maximum payload capability for the vehicle. In this way, the trajectory person also participates in designing the vehicle.

Many authors [1-5] have treated the problem of optimizing the stage propellant loadings of multistage vehicles. None of these authors, however, have attempted to simultaneously optimize the steering program of these vehicles . Others [6-9] have used the calculus of variations approach to optimize the steering program for various rocket vehicles. In particular, Jurovics [9] treats the problem of optimizing the steering program for a multistage launch vehicle. He does not, however, consider the problem of optimizing the stage propellant loading or the kick angle.

Tren and Spurlock [10] have considered the problem of simultaneously optimizing the steering program, propellant loading, and booster kick angle using a variational approach. But in the present study, we simultaneously optimize: (1) the vehicle design variables, nosecone half-angle, vehicle slenderness ratio, and stage propellant loading, and (2) the trajectory parameters, stage burn times, booster kick angle, and steering programs. Ruppe [11], in his paper on design considerations for future launch vehicles, discusses integrating the trajectory model with the vehicle model and propulsion model for optimization of future launch vehicles.

Combined trajectory and vehicle optimization studies have been performed on applications other than launch vehicles also. Wetzel and Moerder, optimize the vehicle and trajectory for aerocapture at Mars [12]. Kluever and Pierson optimize the vehicle and trajectory for a nuclear electric spacecraft for lunar missions [13].

Problem definition

The problem to be solved is to determine the maximum payload capability of a two-stage launch vehicle flown to a low-earth circular orbit of 100 nm. The analysis includes atmospheric effects during first-stage flight but assumes vacuum operation

for the second stage. The trajectory parameters, booster kick angle, stage burn times, steering programs, and the vehicle parameters, nose cone angle, vehicle slenderness ratio, and stage propellant loading are the design variables. This optimal control problem is approximated as a parameter optimization problem, and a sequential quadratic programming (SQP) method is used to solve it.

Literature survey

A mathematically simple but reasonably accurate model to simulate the aerodynamic forces that occur during atmospheric flight was sought. So a survey on the available literature was conducted. The various papers on vehicle sizing were also reviewed. In this section, a review of some of the literature available on aerodynamic modeling, vehicle sizing, and propellant loading for launch vehicles is presented.

Aerodynamic methods for ascent

Steady-state aerodynamic characteristics are provided by various methods in different Mach number regimes. For subsonic incompressible flow, slender body theory [14], which assumes small contour changes, has been used widely to determine the aerodynamic forces. In the transonic regime, linearized theory [15], can be used. For supersonic flows, Van Dyke uses second-order potential theory [16], while Shapiro [17] explains how linearized theory can be used. Syvertson and Dennis [18] employ the generalized shock expansion method to determine the forces for bodies of revolution near zero lift.

The analysis of transonic flow is a complex problem due to the unsteady nature of the flow, the near normal shock waves, and the nonlinear variation of loads with

attitude changes. For these reason, the prediction of aerodynamic loads for Mach numbers near one is not amenable to theoretical methods. The normal approach to transonic aerodynamic problems has been to rely on wind tunnel test results. Hamner, Leff [19] and Thompson [20] give empirical results based on a parametric wind tunnel test of cone-cylinder and cone-cylinder frustum-cylinder configurations with a Mach range of 0.7 to 2.0. The test results define the effects of various nose cone angles, cylinder lengths, frustum angles, and diameter ratios. The total normal force gradient and center of pressure on a vehicle are determined by adding the body of revolution data and the fin and interference data. Perkins and Kuehn, give the variation of the normal force coefficient and center of pressure as a function of angle of attack when they compare experimental and theoretical distributions of lift on a slender inclined body of revolution [21]. The theoretical methods mentioned above are elaborate and require lots of computational time and effort. The empirical results available are restricted to a narrow band of Mach numbers. So for simplicity, empirical relationships which are the results of detailed study of experimental results can be used for preliminary studies. Chin [22] and Cornelisse et al. [23] give such empirical relationships. These empirical relationships are used to model the aerodynamic forces in the present study. This model is described in detail in chapter 2.

Propellant loading

In designing multistage rockets, it is desirable to apportion the weight of the structure and propellant among the various stages in such a manner so as to obtain a minimum gross weight for a given performance. This is known as vehicle sizing. The propellant weight allocated to a stage is known as the propellant loading.

Structure weight represents the fraction of the stage weight that is not usable propellant. Structure factor is a non-dimensional ratio of stage structural weight to the total stage weight. Malina and Summerfield [1] treat the problem of vehicle sizing for the case of a rocket vehicle with an arbitrary number of stages assuming equal structural factor and specific impulse for all stages. Their criterion of performance is the burnout velocity of the last stage which is to be maximized for a given gross take-off weight. Goldsmith [2] treats the case of a two-stage rocket having a different structural factor and specific impulse in each stage. Hall and Zambelli [3] study the optimum weight distribution of multi-stage rockets having different specific impulse and structure factor for each stage. Coleman [4] gives a generalized method for determining the optimum stage weight distribution for multi-stage rockets. He gives a method for taking into account the variations of structural factor with stage weight. Srivastava [5] points out that Coleman's equations are for the case when payload is held constant and terminal velocity is optimized, and he proceeds to give relations for the case when terminal velocity is a constant and payload is optimized.

Structure weight is dependent on the type of propellant, the stage thrust level, and the weight supported by the stage. However, once the design criteria for the stage have been defined to the point that the propellant type and thrust level have been chosen, the major decision is regarding the stage weight. The stage weight depends on the propellant weight, i.e, propellant loading of that stage. Tren and Spurlock [10] approach the problem in a different manner. The structural mass for each stage is assumed to be a function of the stage propellant loading defined by $m_s = m_H + km_p$, where m_s is the total structure mass, m_H is the fixed mass, m_p is the stage propellant mass, and k is the propellant sensitive mass fraction. In the

problem treated here,we assume that the stage structure mass is the sum of the the mass fraction that is sensitive to propellant loading, structural mass which is a function of the stage length and diameter, and a fixed hardware mass. An additional mass fraction which is sensitive to the upper stage mass is added to the first stage. Since propellant mass forms about 90% of the total mass, propellant loading defines the stage length. Hence, here, vehicle sizing is done, wherein the stage propellant loading, stage length, and stage structural weight are optimized along with the upper stage steering program and kick angle. The objective is to maximize the payload capability of the vehicle. Unlike the previous studies, where mass ratios are used, Tren and Spurlock [10] use mass directly for optimization. This method is adopted in the present study, since it is more convenient to use masses than mass ratios while handling several design variables.

CHAPTER 2. MATHEMATICAL MODEL

In this chapter, the system model, the aerodynamic model, and the mass model used in modeling the launch vehicle and its trajectory over a spherical non-rotating Earth are presented. Listed below are the assumptions on which the models are based.

Assumptions

- A spherical non-rotating Earth is assumed. The equations of motion 2.1 assume an inertial frame. Neglecting Earth's rotation means the centrifugal and coriolis forces generated by the transformation of the time derivatives to a rotating frame are neglected. This introduces error in the position and velocity relative to the Earth. An error of 16.3% in payload capability is introduced for a 110-degree launch from the Atlantic Missile Range (AMR) by assuming a non-rotating Earth. This calculation is shown in Appendix-A. The component of velocity due to the Earth's rotation for a 110-degree launch from AMR, v_{rot}, is 1262 ft/sec as presented in Figure 1, chapter 3, by White [24].

- A two-stage vehicle with a simple cone-cylinder configuration of length 160 ft and diameter 23.32 ft is assumed for all cases except when the slenderness ratio is optimized.

- The vehicle is assumed to have constant thrust and specific impulse for every stage.

- A zero wind condition is assumed.

- Thrust vector gimballing is ignored. Hence, the variable α represents both the angle-of-attack and the angle between the thrust and velocity vectors, i.e., $\alpha = \delta$.

- The vertical rise time for the vehicle is chosen to be 13 sec based on Figure 51, chapter 2, by White [24] for a vehicle with an initial thrust to weight ratio of 1.3. Optimization is carried out from the end of the vertical rise phase. The lift-off dynamics is computed separately, and the state variables at the end of 13 sec are assumed to be the initial boundary conditions for the optimization studies. The equations used for the vertical rise segment are given in Appendix-B.

- On average, the first stage burnout takes place around 200,000 ft where the atmospheric density is negligible. Hence, the aerodynamic forces are considered only for the first stage. The second-stage is assumed to operate under vacuum conditions.

- The launch vehicle assumed here is defined by White [24]. The payload is launched into a circular low Earth orbit of 100 nm as specified by White [24]. The propulsion and weight data are given in Appendix-C [24]. This orbit lies well below the Van Allen belt. Van Allen radiation belts are regions of trapped high-flux, high-energy particles - protons and electrons of both solar and cosmic origin. While the belts provide a severe radiation environment for space vehicles

traveling through them, they do to some extent protect low orbiting vehicles from sources of external particulate radiation.

System model

The vehicle dynamics are the standard planar, point-mass equations of motion over a non-rotating, spherical Earth with inverse-square gravity field and a stationary, exponential atmosphere [25]. The state variables are velocity v, flight path angle γ, surface range s, and altitude h. The geometric situation is as shown in Figure 2.1. The equations of motion are

$$\frac{dv}{dt} = \frac{(Tcos\alpha - D)}{m} - gsin\gamma \tag{2.1}$$

$$v\frac{d\gamma}{dt} = \frac{(Tsin\alpha + L)}{m} - (g - \frac{v^2}{r})cos\gamma \tag{2.2}$$

$$\frac{ds}{dt} = (\frac{R}{r})vcos\gamma \tag{2.3}$$

$$\frac{dh}{dt} = vsin\gamma \tag{2.4}$$

where $g(h) = g_s[\frac{R}{R+h}]^2$ is the acceleration due to gravity at altitude h, $r = h + R$ gives the vehicle distance from the Earth's center, and R denotes the Earth's radius. The pitch angle, $\theta = \gamma + \alpha$, will be used as the control variable. We assume no gimballing of the engines, so that the thrust vector is always directed along the vehicle centerline.

Aerodynamic model

Simple empirical formulae are used to estimate the aerodynamic forces. These forces, lift and drag, may be classified into two general types: one, due to air friction and the other due to pressure. The pressure forces can further be classified into base

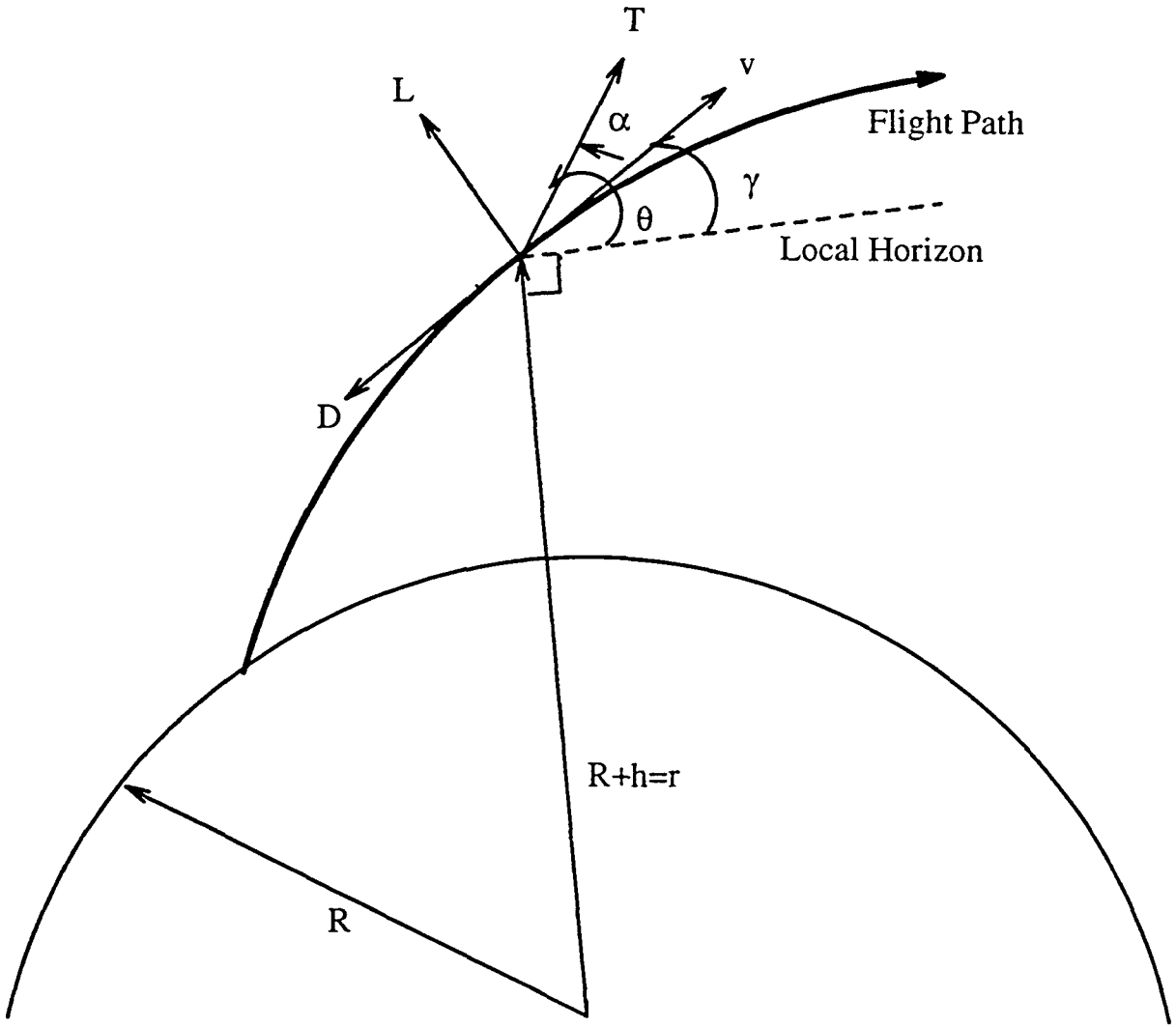

Figure 2.1: Planar Ascent from Non-rotating Earth

pressure and pressure forces on the vehicle body. In launch vehicle studies, it is more convenient to consider normal forces, i.e., the forces perpendicular to the vehicle axis, in lieu of lift forces. For a simple cone-cylinder configuration, the above three factors are analyzed for the cone and the cylinder separately, neglecting interference effects. Since the aim is to get a simple but fair estimate of the aerodynamic forces, approximations are made wherever possible.

Pressure forces

The vehicle travels through subsonic, transonic and supersonic Mach regimes. Since these three regimes have different flow characteristics, the aerodynamic forces are calculated separately for each flow region.

In subsonic flow, pressure forces are small and thus can be neglected. In the transonic region, the highly mathematical transonic area rule [26] has to be used. Since the launch vehicle encounters this region for only a very short time, we will neglect transonic pressure forces. In the supersonic region, pressure variations on the nosecone are substantial while the pressure forces on the cylinder are negligible. Described below are the pressure forces on the nosecone and the cylinder.

- Nosecone: The axial and normal force coefficients C_A and C_N on the nosecone are a function of the Mach number M, the nosecone half-angle σ, and angle-of-attack α and are given by [22]

$$C_A = (0.083 + \frac{0.096}{M^2})(\frac{\sigma}{10})^{1.69} \tag{2.5}$$

$$C_N = C_{N\alpha}\alpha \tag{2.6}$$

$$\text{where}, C_{N\alpha} = \frac{2\sqrt{\frac{cot\sigma}{\sqrt{M^2-1}}^2 - 1}}{\frac{\sqrt{M^2-1}}{cot\sigma} cosh^{-1} \frac{cot\sigma}{\sqrt{M^2-1}} + \sqrt{\frac{cot\sigma}{\sqrt{M^2-1}}^2 - 1}} \tag{2.7}$$

$$\text{and}, M = \frac{v(t)}{a(h)} \tag{2.8}$$

Density variation with altitude is given by [27]:

$$\rho(h) = \rho_0 e^{\frac{-h}{h_1}} \tag{2.9}$$

where $\rho_0 = 2.54\text{x}10^{-3} slug/ft^3$ and $h_1 = 2.73\text{x}10^4 ft$.

For speed of sound, a, we have [27]:

$$a(h) = \begin{cases} (k_1 - k_2 h)^{1/2} & \text{if h}\leq \text{ 36,000 ft} \\ 968.1 ft/sec & \text{if h}> \text{ 36,000 ft} \end{cases} \tag{2.10}$$

where $k_1 = 1.244\text{x}10^6 ft^2/sec^2$, and $k_2 = 8.57 ft/sec^2$.

- Cylinder: At zero angle of attack, the pressure contribution to lift and drag is zero. At small angles of attack, there is a small normal force due to the carry over from the nose. This effect is negligible. At large angles of attack, some amount of normal force is developed because the cross flow drag acts normal to body center line. Large angles of attack occur during lift-off with wind. Since optimization begins from the end of the lift-off phase (i.e., after 13 sec of vertical flight) and no wind is assumed, this effect is ignored.

Base pressure

This forms a substantial part of the drag for jet-off conditions. For powered flight, the engine mass flow interacting with the base and external flow completely

modifies power-off base drag. Engine ignition and vehicle lift-off induce a phenomenon called base aspiration. This effect is diminished as the vehicle leaves the launch pad and is negligible when the vehicle is five or six diameters from the pad. This short period is generally neglected in preliminary design. For supersonic flight, power-on drag may be determined by calculating the interaction of plume and free-stream Mach number, exit pressure, engine flow characteristics, and the geometry of the engine and the base. Optimization studies performed, as explained in the subsequent chapters, indicate that the optimal payload reduces by less than 1% when base drag is included in the aerodynamic model. Appendix-D gives the comparison of optimization studies with and without base drag. Due to the complexity of the mathematical calculations involved and the small magnitude of this drag, base drag is neglected in this study for all cases except when slenderness ratio is optimized. When slenderness ratio is optimized, the base-pressure drag coefficient C_{D_b} is calculated from base-pressure coefficient C_{P_b} under jet-on condition as follows:

$$C_{D_b} = C_{P_b} \frac{S_b}{S} \tag{2.11}$$

where, S_b is the effective base area as shown by the shaded region in Figure 2.2, S is the body cross-sectional reference area and C_{P_b} is the base-pressure coefficient as given in Figure 2.3 as a function of Mach number by Chin [22].

Skin friction force

Finally, the contribution of skin friction in the three flow regions, namely subsonic, transonic and supersonic is considered.

- Subsonic Flow: In subsonic flow, friction drag is over 90 per cent of the total force and is primarily a function of the type of flow (laminar or turbulent) and

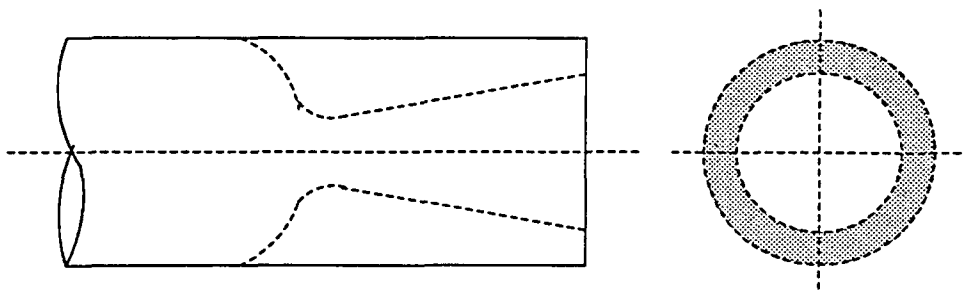

Figure 2.2: Effective Base Pressure Area For Calculation of Base Drag

the total wetted area. The skin friction coefficient in laminar flow is given by Blasius's equation [22]

$$C_{fL} = \frac{1.328}{\sqrt{Re}} \tag{2.12}$$

For turbulent incompressible flow, the Ka'rm'an-Schoenherr equation gives the friction coefficient as [22]

$$\sqrt{C_{fT}} log_{10} C_{fT} Re = 0.242 \tag{2.13}$$

where Reynolds number is given by $Re = \frac{\rho v l}{\mu}$.

For most flight conditions laminar flow prevails over the front portion of the vehicle body, followed by completely turbulent flow over the remaining portion of the body [22]. Because of the complex nature of the flow and the interaction effects of factors such as pressure gradient, surface smoothness and Reynold's number, there is no useful theoretical method which can predict this transition point [22]. In general the transition point of a smooth and streamlined body may be located as far back as 30 per cent of its length. For a cone-cylinder configuration, considering the cone-cylinder intersection point as a transition point is a fairly valid assumption. In other words, the flow over the cone section is assumed to be laminar and the flow over the cylinder is assumed to

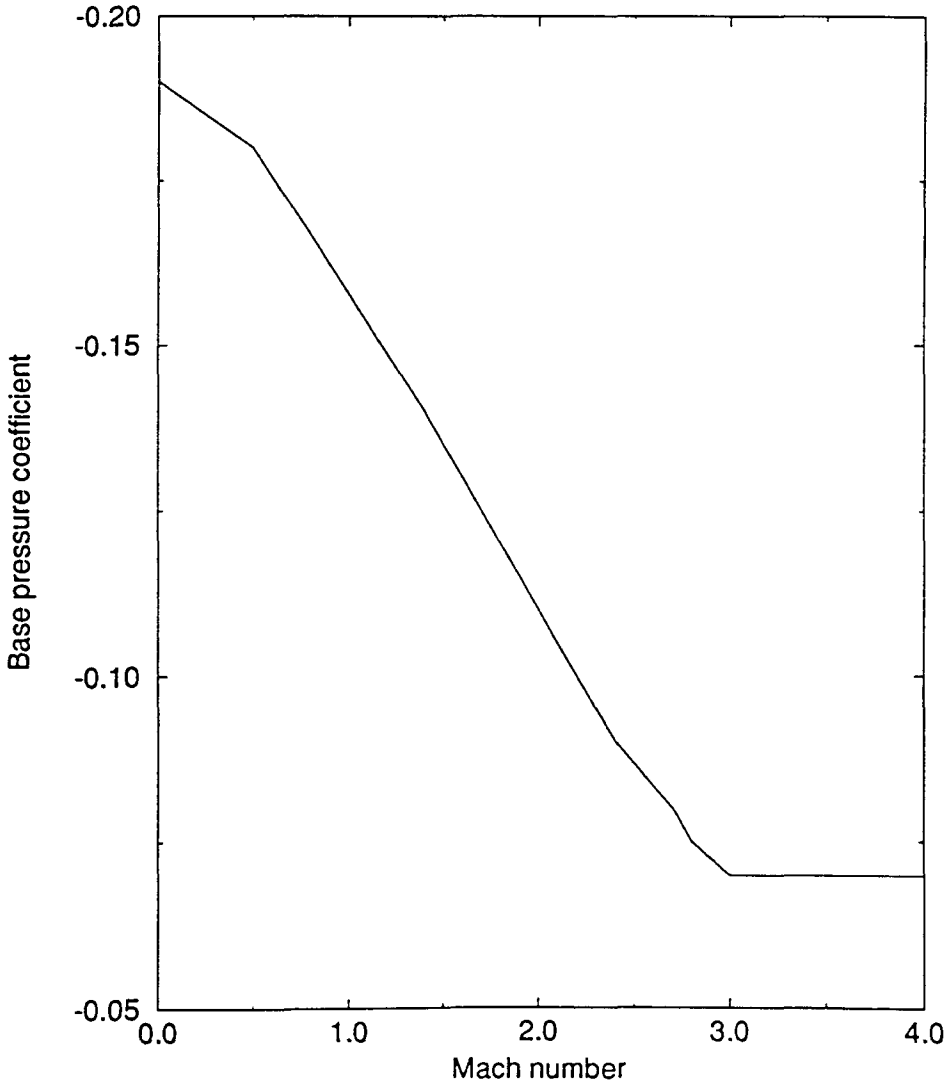

Figure 2.3: Base-Pressure Coefficient vs. Mach Number

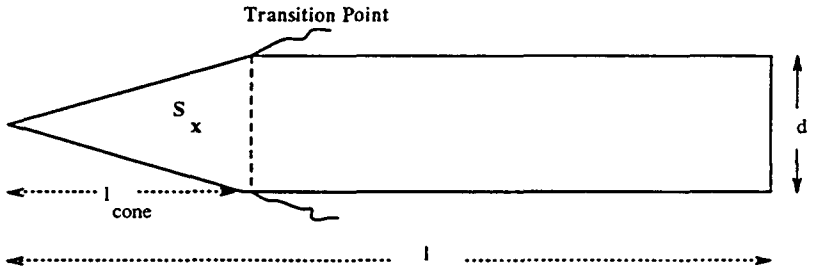

Figure 2.4: Transition Point for Calculation of Skin Friction Drag

be turbulent. Hence, it follows that the skin-friction coefficient for the vehicle is given by [22]

$$C_f = C_{fL}\frac{S_x}{S_L} + C_{fT}\frac{S_L - S_x}{S_L} \tag{2.14}$$

where, S_x is the wetted area over cone length l_{cone} and S_L is the total wetted area over length l as shown in Figure 2.4.

- Transonic and Supersonic flow: For transonic and supersonic regions (when M $\geq$ 1), compresibility effects have to be taken into account. When the flow is laminar, the effect of compresibility reduces the skin-friction coefficient [22] by:

$$\frac{C_f}{C_{f0}} = \left(\frac{1}{1 + 0.85\frac{M^2}{5}}\right)^{0.1295} \tag{2.15}$$

where, C_{f0} is the skin-friction coefficient in laminar incompressible flow as given by equation 2.12 When the flow is turbulent,

$$\frac{C_f}{C_{f0}} = \frac{1}{(1 + \frac{\gamma-1}{2}M^2)^{0.467}} \tag{2.16}$$

where, C_{f0} is the skin-friction coefficient in turbulent incompressible flow as given by equation 2.13. The total skin friction drag can be found using equation 2.14.

The drag coefficient can be obtained by dividing the skin friction coefficient by the ratio of wetted area to reference area [22].

$$C_{Dskinfriction} = C_f \frac{S_{wetted}}{S} \tag{2.17}$$

Lift and drag forces

From the axial and normal forces, the total drag and lift forces are given by

$$D = \frac{\rho v^2 S}{2}((C_N sin\alpha + C_A cos\alpha)_{cone} + C_{Dskinfricion} - C_{D_b}) \tag{2.18}$$

$$L = \frac{\rho v^2 S}{2}(C_N cos\alpha - C_A sin\alpha)_{cone} \tag{2.19}$$

Vehicle Sizing

The vehicle is assumed to be 160 ft long with a diameter of 23.32 ft. The diameter is calculated from the given reference area [24]. Based on the given specific impulse, it is assumed that the first stage is loaded with liquid oxygen oxidizer and RP-1 fuel in the weight ratio 2.2:1, and the second stage propellant mixture to be liquid oxygen oxidizer and liquid Hydrogen fuel in the weight ratio 5:1. Based on the propellant mass loaded in the first stage m_{propl}, the stage length is calculated as follows:

$$l_1 = \frac{vol_1}{\pi r^2} \tag{2.20}$$

$$\text{where, } vol_1 = \frac{70.84 m_{propl}}{228.416} + \frac{32.2 m_{propl}}{161.536} \tag{2.21}$$

The second stage length due to propellant loading m_{prop2} is given by:

$$l_2 = \frac{vol_2}{\pi r^2} \tag{2.22}$$

$$\text{where, } vol_2 = \frac{161 m_{prop2}}{428.28} + \frac{32.2 m_{prop2}}{26.52} \tag{2.23}$$

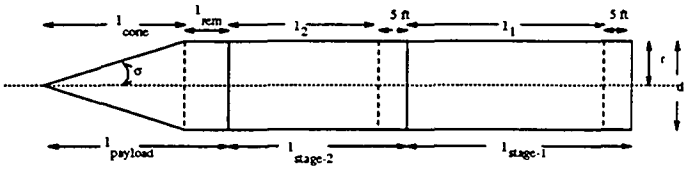

Figure 2.5: Vehicle Configuration

These relationships are derived in Appendix-E.

An additional constant length of 5 ft is assumed for each stage to account for the hardware. Hence, length of stage I $= l_1 + 5$, and length of stage II $= l_2 + 5$. Since the total length is assumed to be 160 ft for all cases except when slenderness ratio is optimized, the remaining cylinder length i.e., $l_{rem} = 160 - l_1 - l_2 - l_{cone} - 10$ is assumed to house the payload along with the conical section.

Mass, propellant loading and payload

Since the propellant flow rate for each stage is a constant, the instantaneous mass m_i of the i-th stage can be expressed as a linear function of the burning times of the stages $\tau_i = t_i - t_{ig}$ as [10]:

$$m_i = m_0 - \beta_i \tau_i \tag{2.24}$$

where, β_i is the propellant flow rate of that stage, m_0 is the initial mass of the stage, and t_{ig} is the ignition time of that stage. The total mass of the vehicle is composed of the structural mass m_{stru}, propellant mass m_{prop} and payload mass m_{PL}.

$$m_{lift-off} = m_{prop1} + m_{stru1} + m_{prop2} + m_{stru2} + m_{cone} + m_{PL} \tag{2.25}$$

The propellant mass of the two stages are given by:

$$m_{prop1} = \beta_1(t_1 - t_0) \tag{2.26}$$

$$m_{prop2} = \beta_2(t_f - t_1) \tag{2.27}$$

The structural mass of the two stages are as given below:

$$m_{stru1} = m_{engine1} + m_{shell1} + m_{upper} + m_{prop-sens1} \tag{2.28}$$

$$m_{stru2} = m_{engine2} + m_{shell2} + m_{prop-sens2} \tag{2.29}$$

where,

- m_{engine} is fixed for the two stages and is independent of vehicle sizing. Based on Saturn-IB, which is a two-stage vehicle and has similar propulsion characteristics [28] to our assumed vehicle, stage I is assumed to have two Rocketdyne H-1 engines and stage II is assumed to have nine Rocketdyne J-2 engines. The propulsion and weight characteristics of these engines are given in Appendix-F.

- m_{shell} is the mass of the cylindrical shell of the stage and is a function of the radius and length of the stage. The shell is assumed to be 0.5 inches thick and made of aluminum casing. m_{shell} is calculated from the density of aluminum and the volume of the shell. Density of aluminum is 5.23852 $slug/ft^3$.

$$m_{shell1} = \rho_{Aluminum}\pi((r+t)^2 - r^2)(l_1 + 5) \tag{2.30}$$

$$m_{shell2} = \rho_{Aluminum}\pi((r+t)^2 - r^2)(l_2 + 5) \tag{2.31}$$

  Here, r is the radius of the stage, and l_1 and l_2 are the stage lengths due to propellant loading and are calculated using equations 2.20 and 2.22.

- m_{upper} is the penalty mass added to the first stage for any increase in the upper stage mass. In other words, this is the additional first stage structural mass required to support the upper stages. m_{upper} is assumed to be 3% of the upper stage mass. Here, by upper stage, we mean the mass of the second stage and the payload mass.

- $m_{prop-sens}$ accounts for the propellant mass fraction that is sensitive to propellant loading. $m_{prop-sens} = km_{prop} = k\beta\tau$ where k is the propellant sensitive fraction and m_{prop} is the propellant mass. k is assumed to be 3% for stage I and 2% for stage II [10].

Hence, we have,

$$m_1{}^0 = m_0 \tag{2.32}$$

$$m_1{}^f = m_0 - (1+k_1)\beta_1\tau_1 - m_{engine_1} - m_{upper} - m_{shell1} \tag{2.33}$$

$$m_2{}^0 = m_1{}^f \tag{2.34}$$

$$m_2{}^f = m_2{}^0 - (1+k_2)\beta_2\tau_2 - m_{engine_2} - m_{shell2} \tag{2.35}$$

where, the superscripts 0 and f refer to conditions at the beginning and the end of each stage, respectively, and the subscript refers to the stage. The final payload is given by

$$m_{PL} = m_2{}^f - m_{cone} \tag{2.36}$$

where m_{cone} is the mass of the cone-cylinder shell that houses the payload. m_{cone} is calculated using the volume of the shell and density of aluminum as:

$$m_{cone} = \rho_{Aluminum}\frac{\pi((r+t)^2 - r^2)l_{cone}}{3} + \pi((r+t)^2 - r^2)l_{rem} \tag{2.37}$$

Transformation to a fixed end-time problem

The final time t_f is not a fixed value, but varies according to when the vehicle achieves orbital conditions. This presents a problem since the performance index is a function of the final time. A linear time transformation is used to convert the free-end time optimal control problem into a fixed end-time problem. If we assume a non-dimensional time variable τ which varies over the interval $\frac{t_0}{t_f} \leq \tau \leq \frac{t_1}{t_f}$ for the first stage and over $\frac{t_1}{t_f} \leq \tau \leq 1$ for the second stage, we can write the linear time transformation

$$t = \alpha_t \tau \tag{2.38}$$

where $\alpha_t = t_f$, t_0 is the time when pitch over begins, and t_1 is the first-stage burn-out time. The transformed equations of motion can now be integrated over the fixed interval $[\frac{t_0}{t_f},1]$, and α_t can be added to the vector of design variables where it can vary along with the other control variables.

Optimal control problem statement

Two class of problems are solved. In class I, the first-stage assumes a gravity turn, wherein only second stage pitch angle history $\theta_2(\tau)$ is optimized, while in class II type of problems, both first and second stage pitch angle histories $\theta_1(\tau)$ and $\theta_2(\tau)$ are optimized.

The formal problem statement for the baseline optimal control problem of class I where only the second-stage pitch angle history and the stage burn times are optimized can be stated as follows:

Find the second-stage pitch angle time history $\theta_2(\tau), \frac{t_1}{t_f} \leq \tau \leq 1$, and the control

parameters, stage I burn-time t_1 and stage II burn-out time t_f, which minimize

$$J = -m_{PL} = \begin{cases} -(m_0 - \beta_1(t_1 - t_0) - m_{stru1}(t_1) - \beta_2(t_f - t_1) \\ -m_{stru2}(t_1, t_f) - m_{cone}(t_f)) \end{cases} \tag{2.39}$$

subject to

$$\frac{dv}{d\tau} = [\frac{(Tcos\alpha - D)}{m} - gsin\gamma]t_f \tag{2.40}$$

$$v\frac{d\gamma}{d\tau} = [\frac{(Tsin\alpha + L)}{m} - (g - \frac{v^2}{h+R})cos\gamma]t_f \tag{2.41}$$

$$\frac{dh}{d\tau} = vsin\gamma t_f \tag{2.42}$$

$$\tag{2.43}$$

for $0 \leq \tau \leq 1$, with initial conditions

$$v(0) = 149.89 \text{ ft/sec} \tag{2.44}$$

$$\gamma(0) = 89.7 \text{ deg} \tag{2.45}$$

$$h(0) = 886.09 \text{ ft} \tag{2.46}$$

with final conditions,

$$v(t_f) = \sqrt{\frac{\mu}{h(t_f) + R}} \tag{2.47}$$

$$\gamma(t_f) = 0 \tag{2.48}$$

$$h(t_f) = 100 \text{ nm} \tag{2.49}$$

and inequality constraints,

$$m_{PL} > 0 \tag{2.50}$$

$$l \geq l_{stage-I} + l_{stage-II} + 10 + l_{cone} \tag{2.51}$$

$$\frac{m_{PL}}{\rho_{PL}} \leq \frac{\pi r^2 l_{cone}}{3} + \pi r^2 l_{rem} \tag{2.52}$$

where, $l_{rem} = l - l_{stage-I} - l_{stage-II} - l_{cone}$

and instantaneous mass:

$$m(\tau) = \begin{cases} m_0 - \beta_1 \tau, & 0 \leq \tau \leq \frac{t_1}{t_f} \\ m_{02} - \beta_2 \tau, & \frac{t_1}{t_f} \leq \tau \leq 1 \end{cases} \tag{2.53}$$

where m_0 is the mass at the begining of pitch over phase, and m_{02} is the mass of the vehicle at second-stage ignition.

The optimal control problem statement for the final class II problem where the trajectory design variables: pitch angle history of both stages, stage burn times, kick-angle and the vehicle design variables: slenderness ratio, nosecone half-angle are optimized can be stated as follows:

Find the stage I burn-time t_1, stage II burn-out time t_f, kick-angle κ, vehicle diameter d, length l, half-angle of the nosecone σ and pitch angle histories $\theta_1(\tau)$, $\frac{t_0}{t_f} \leq \tau \leq \frac{t_1}{t_f}$ and $\theta_2(\tau)$, $\frac{t_1}{t_f} \leq \tau \leq 1$, which minimize

$$J = m_{PL} = \begin{cases} -(m_0 - \beta_1(t_1 - t_0) - m_{stru1}(t_1, l, d) - \beta_2(t_f - t_1) \\ -m_{stru2}(t_1, t_f, l, d) - m_{cone}(\sigma, t_f, l, d)) \end{cases} \tag{2.54}$$

subject to

$$\frac{dv}{d\tau} = [\frac{(T cos\alpha - D)}{m} - g sin\gamma] t_f \tag{2.55}$$

$$v\frac{d\gamma}{d\tau} = [\frac{(T sin\alpha + L)}{m} - (g - \frac{v^2}{h+R}) cos\gamma] t_f \tag{2.56}$$

$$\frac{dh}{d\tau} = [v sin\gamma] t_f \tag{2.57}$$

for $0 \leq \tau \leq 1$, with initial conditions

$$v(0) = 149.89 \text{ ft/sec} \tag{2.58}$$

$$\gamma(0) = 90.0 - \kappa \text{ deg} \tag{2.59}$$

$$h(0) = 886.09 \text{ ft} \tag{2.60}$$

with final conditions,

$$v(t_f) = \sqrt{\frac{\mu}{h(t_f)+R}} \tag{2.61}$$

$$\gamma(t_f) = 0 \tag{2.62}$$

$$h(t_f) = 100 \text{ nm} \tag{2.63}$$

and inequality constraints,

$$m_{PL} > 0 \tag{2.64}$$

$$l \geq l_{stage-I} + l_{stage-II} + 10 + l_{cone} \tag{2.65}$$

$$\frac{m_{PL}}{\rho_{PL}} \leq \frac{\pi r^2 l_{cone}}{3} + \pi r^2 l_{rem} \tag{2.66}$$

where, $t_0 = 13$ sec, $l_{rem} = l - l_{stage-I} - l_{stage-II} - l_{cone}$.

Since the range equation (2.3) is uncoupled from the rest of the system equations, it is not included in the dynamics. The range history is later obtained by integrating the range equation using the optimized design values. The optimal control problem is handled in two segments since the dynamics of the two stages are different. The above listed dynamics hold for the first stage, while for the second stage, lift and drag are zero, i.e., $D = 0$ and $L = 0$. At the end of the first-stage burnout, the first-stage structural mass is removed, and the updated state variable values are taken as the initial values for the second-stage state variables.

CHAPTER 3. SOLUTION METHOD

This chapter presents the numerical method that is used to solve the optimal control problem.

Direct approach

The general optimal control problem statement can be written as follows: Find the control time history u(t), $t_0 \leq t \leq t_f$, which minimizes the performance index:

$$J = \phi[\vec{x}(t_f)] + \int_{t_0}^{t_f} L(\vec{x}, u, t)\, dt \tag{3.1}$$

subject to the differential state equation constraints:

$$\dot{\vec{x}} = \vec{f}(\vec{x}, u, t), \vec{x}(t_0) = \vec{x}_0 \tag{3.2}$$

and the control inequality constraints:

$$u_{min} \leq u(t) \leq u_{max} \tag{3.3}$$

and the terminal state constraints:

$$\psi(\vec{x}, u) = 0 \tag{3.4}$$

The optimal control problem can be solved either by using a direct method or an indirect method. In direct methods, also called gradient methods, the control

values are guessed and the state equations are integrated forward while the costate equations are integrated backward. The function space gradient of J, H_u, is identified ($dJ = \int_0^T H_u^T \delta u dt$) and the control is updated $u(t)_{new} = u(t)_{old} + \alpha(-H_u)$. This procedure is iterated until $H_u = 0$. In indirect methods, the necessary conditions for optimality are applied to the problem, and the resulting two-point boundary value problem is solved. Shooting methods and quasi-linearization methods are two of the indirect methods available. This approach has two drawbacks. First, due to the analytical work involved in deriving the costate equations and the influence function equations, the initial preparation time to set up the problem is high. Second, the problem must be defined analytically in order that these infinite-dimensional methods can be implemented. This is not always possible.

In both the direct and indirect approaches, the function-space problem can be approximated by a finite-dimensional problem and solved as a nonlinear programming problem. Rather than minimizing the performance index over the entire control history, we now minimize over a fixed set of control parameters. The performance index evaluation usually requires the numerical integration of the equations of motion constraints and then the numerical or explicit evaluation of the performance index and constraints. Thus, an approximate solution to the infinite-dimensional optimal control problem is found by varying the finite set of variables resulting from the discretized control using a nonlinear minimization method.

In the present study, a direct method replaces the optimal control problem with an approximate nonlinear programming problem. This nonlinear programming problem replaces the infinite-dimensional control time history, u(t), with a cubic spline or linear fit through a finite set of control parameters. Figure 3.1 shows a graphical

example of this discretization on a simple control history. The performance index is payload, which is a variable not an integral. So the performance index is evaluated explicitly. The control variables include both discrete and continuous trajectory and vehicle design variables. First and second-stage burn times, booster kick angle, half-angle of the nose cone, and vehicle slenderness ratio are the discrete design variables, while the pitch programs are the continuous variables. The continuous variables are parameterized by a cubic spline interpolation through a fixed number of equally-spaced variables. The number of variables is chosen by trial and error such that the behavior of the function is completely represented, and increasing the number of variables further has no effect on the performance and the trend of the function. The pitch program for each stage is parameterized by twenty five control points. Linear interpolation is also used to verify the results. Though linear interpolation scheme is faster, it does not accurately reflect a continuous control without a large number of control points. So, in order to decrease the computational burden but still retain accuracy, cubic spline interpolation is used. The nonlinear minimization method used for solving the nonlinear problem is sequential quadratic programming (SQP).

Sequential quadratic programming

The sequential quadratic programming algorithm is a constrained Quasi-Newton method which finds the solution to the nonlinear programming problem by solving a sequence of quadratic programming problems. Quadratic programming problems are parameter optimization problems with a quadratic objective function and linear constraints. The solution of the quadratic programming problem is equivalent to the solution of the linearized necessary conditions for the nonlinear problem. Therefore,

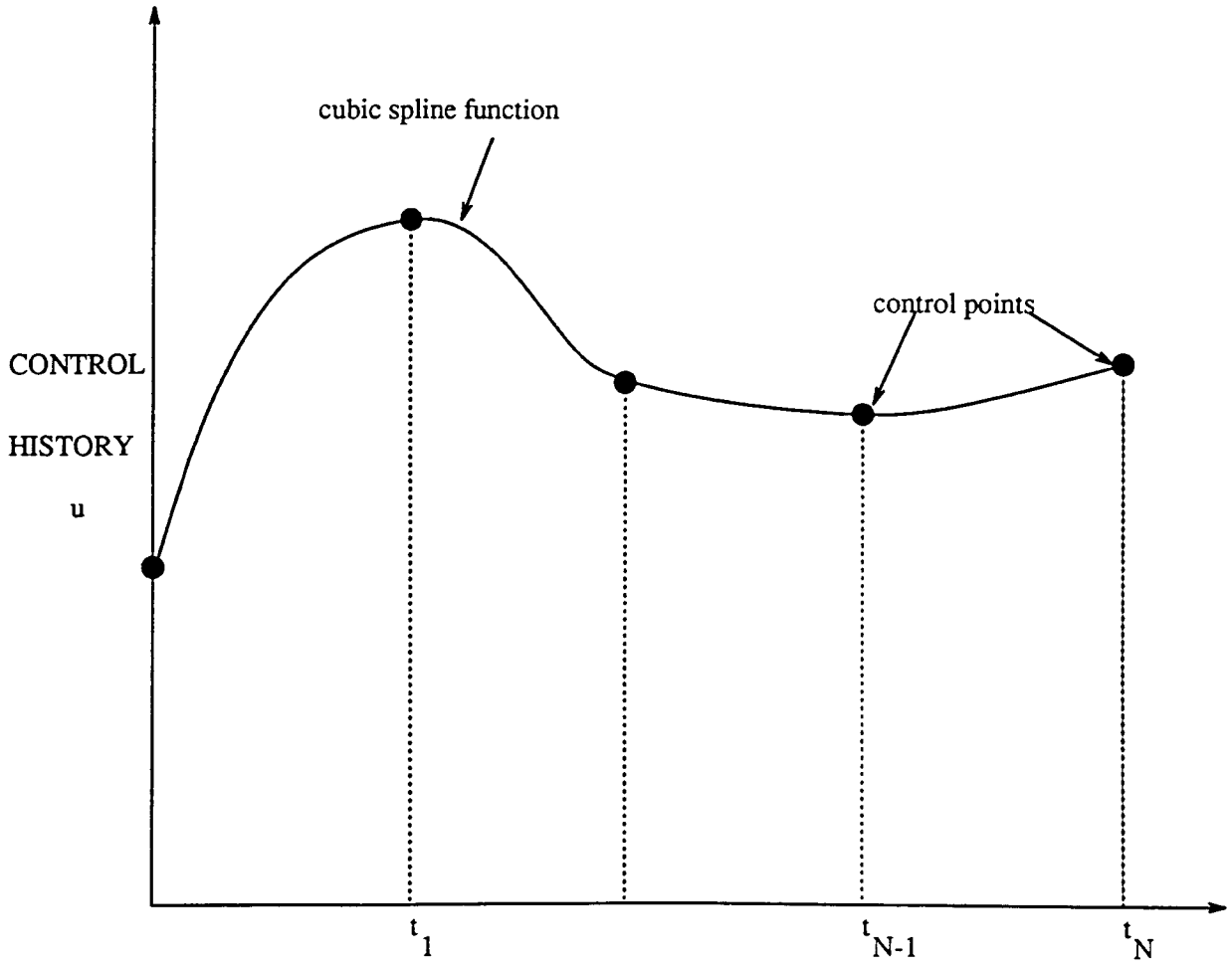

Figure 3.1: Discrete Parameterization of u(t)

the approximate nonlinear programming problem is solved by solving a sequence of quadratic programming problems. The basic sequential quadratic programming algorithm is composed of four steps:

a. Estimate the Hessian matrix for the Lagrangian function and the vector of problem variables. The initial Hessian estimate must be positive-definite. Compute the partial derivatives of the performance index and constraints with respect to the control parameters via numerical integration and finite difference equations.

b. Solve a quadratic programming problem for the corrections to the control parameter vector and the corresponding Lagrange multipliers. The correction vector gives the direction of search.

c. Perform a step-size selection based on some function which measures changes in the objective function and constraints with the correction vector as the direction of search. This step is used to force convergence from poor initial guesses of the control parameter vector.

d. Update the control parameter vector with the step-size value and the resulting correction vector. Compute a new trajectory and test the termination criteria for convergence. Update the Hessian matrix with a variable-metric formula to ensure that the Hessian estimate stays positive-definite.

A Runge-Kutta method is used to integrate the equations of motion. This is described in more detail in Appendix G.

CHAPTER 4. VALIDATION OF AERODYNAMIC MODEL AND DISCUSSION OF RESULTS

Validation of aerodynamic model

Based on the C_d curve presented by White [24], a launch vehicle of length 160 ft and diameter 23.32 ft is assumed for the purpose of validating the aerodynamic model. This chosen vehicle has a simple cone-cylinder configuration and can be classified along with the Saturn-IB series based on its dimensions. Various half-cone angles between 20 deg and 45 deg are used.

Comparison of the C_d vs M history generated by the model with the C_d curves assumed by White [24] shows that the trend agrees fairly well in the supersonic region, while it differs in the subsonic region as shown by Figure 4.1. This is justifiable under the assumptions made that the base drag and the normal cross flow force are negligible. Normal cross flow force is a major contributor towards the drag force at large angles of attack in the subsonic region. In most trajectory studies, constant aerodynamic coefficient values are assumed for preliminary analysis. For example, Mackay and Weber [29] assume a constant C_d value of 0.4 and zero C_L in their performance studies on various multi-stage boosters. This value has been quoted [29] to be typical for current launch vehicles. The aerodynamic model considered here gives a fairly good approximation of the actual aerodynamic characteristics as shown

in Figure 4.1 and is much better than assuming constant characteristics. Hence, it is used for the present optimization studies.

Figure 4.2 shows the C_d vs Mach number profile for various nosecone half-angles σ for a 160 ft vehicle. It can be seen from Figure 4.3 that the effect of varying the vehicle length on the drag coefficient is negligible since skin-friction is a very small percentage of the total drag. Symbols are used to distinguish the various cases in Figures 1.2 and 1.3.

Hierarchy of problems

The motivation behind this study is to integrate trajectory and vehicle design optimization. The problem considered is to maximize the payload of a two-stage launch vehicle, flown to a circular orbit of 100 nm. The parameters and functions free for optimization are the stage burn time, booster kick angle, stage propellant loading, vehicle nosecone half-angle, vehicle slenderness ratio, and pitch program. This is carried out by formulating and successively solving a hierarchy of problems. Each subsequent problem has additional control variables and is more complex than the preceding problem, and its solution provides valuable information for solving the next problem. Two classes of problems are treated. In the first one, the first-stage pitch program is assumed to be completely specified ("gravity turn" with zero angle-of-attack and therefore $\theta = \gamma$), while in the second one, the first-stage pitch program is also available for optimization. The gravity turn model is used in many launch trajectories to reduce the maximum dynamic pressure level that occurs during atmospheric flight and the large transverse structural loads that occur at large angles-of-attack.

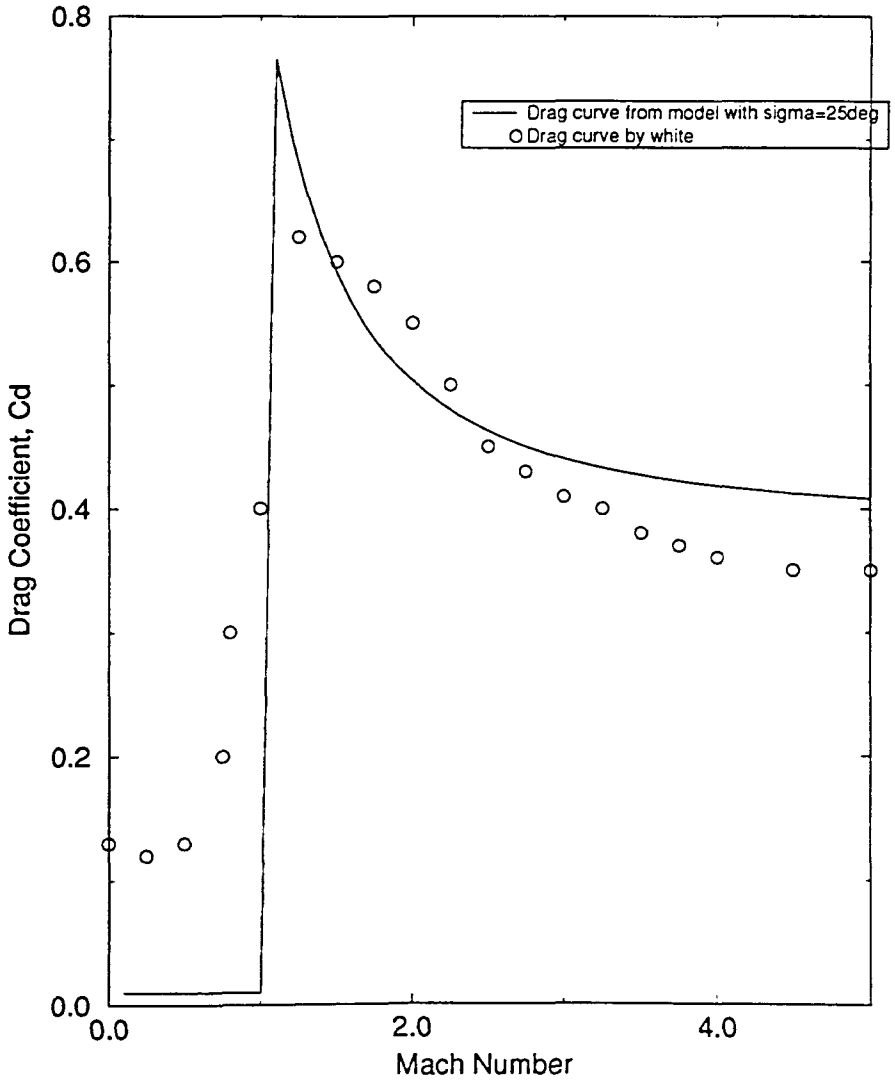

Figure 4.1: Comparison of C_d vs M Profiles

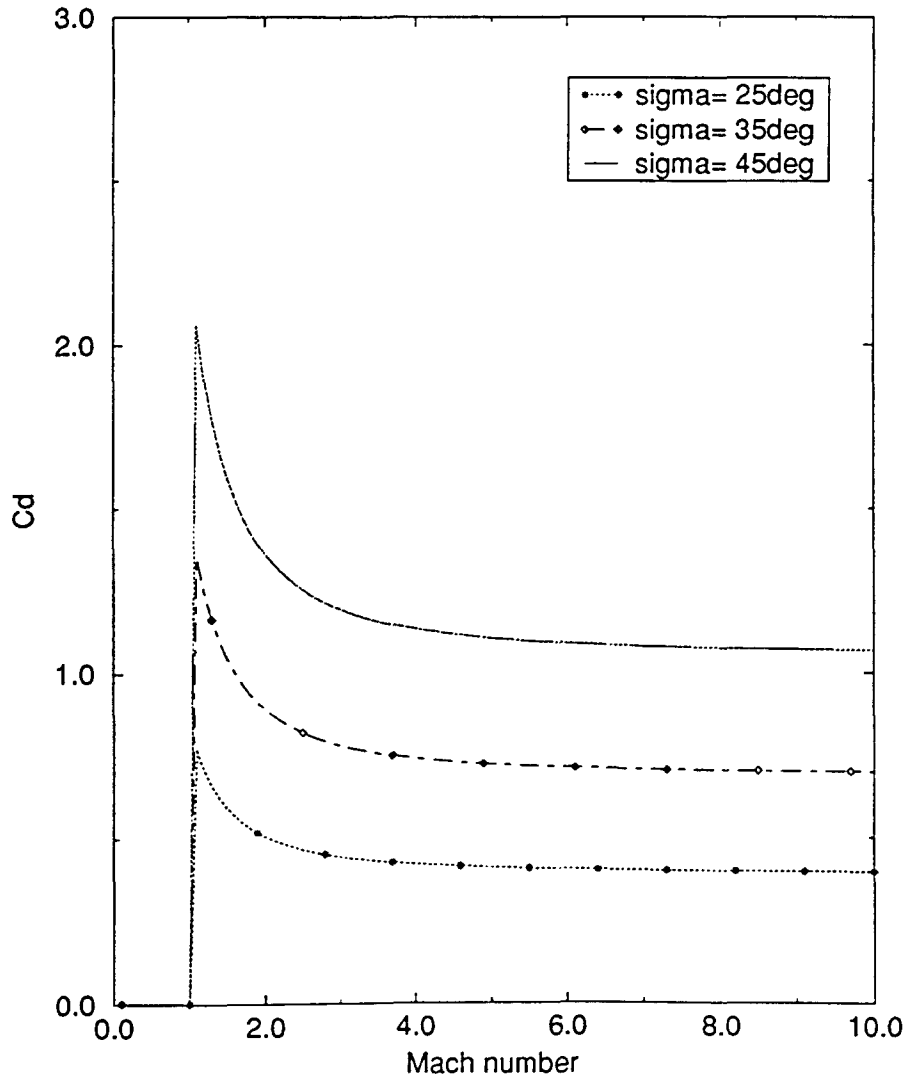

Figure 4.2: Drag Coefficient C_d vs Mach Number for a Vehicle of Length 160 ft Using the Assumed Aerodynamic Model

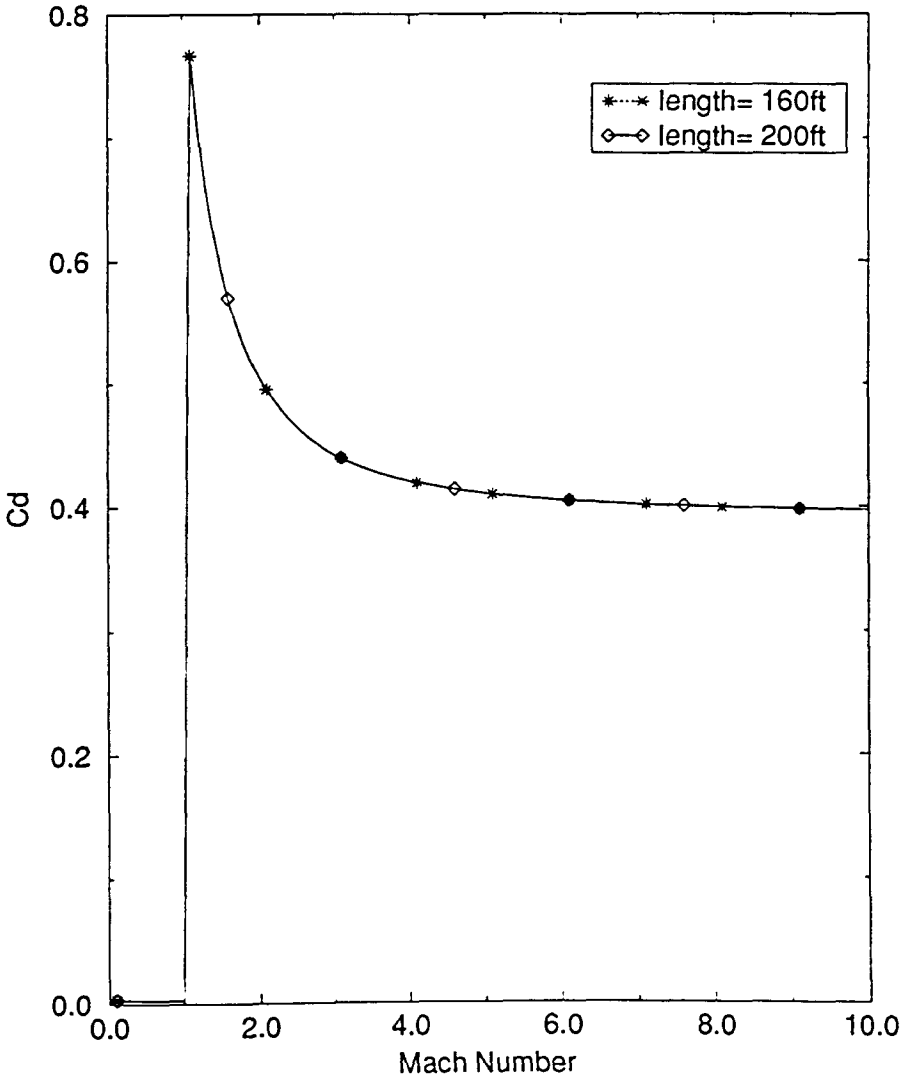

Figure 4.3: Drag Coefficient C_d vs Mach Number for a Vehicle With σ=25 deg

Class-I problems

This class of problems assumes a gravity turn for the first stage, while the second-stage pitch program is unconstrained and is determined to maximize the payload. The following cases are optimized. First, a baseline problem (case 1) is established in which a simple cone-cylinder vehicle configuration, with a constant drag coefficient $C_d = 0.4$ and a booster kick angle of 0.3 deg, is considered. A constant value of 0.4, which is typical of current vehicles [29], is used for the drag coefficient C_d during first-stage flight. The stage I structural mass that is thrown out at first stage burn-out is assumed to be 10% of the stage weight. The second-stage pitch program and the stage burn times are optimized. In case 2, the 10% structural mass is split into a mass fraction that is sensitive to propellant loading and a fixed hardware mass. The propellant sensitive mass fraction is assumed to be 3% of the propellant loaded in stage I and 2% for stage II. The second-stage pitch angle history is discretized using twenty five control variables. So, in the baseline problem, twenty seven control variables are optimized.

Next, the booster kick angle is set free (case 3). An angle of 0.05 deg is given as the lower boundary for this design variable. The trajectory is very sensitive to this parameter. The constant aerodynamic characteristics $C_d = 0.4, C_L = 0.0$, are then replaced by a variable aerodynamic profile which is generated by the aerodynamic model described in chapter 3 (case 4). This model uses a nosecone half-angle of 25 deg. Next, the half-angle of the nosecone is allowed to be optimized (case 5). Chin [22] states that the vehicle weight increases drastically below a half-cone angle of 15 deg. Bluff shapes have poor aerodynamic lifting performance. Hence, a lower limit of 15 deg and an upper limit of 45 deg are fixed as the control boundaries for

the half-angle of the nosecone.

Class-II problems

In the second class of problems, the baseline problem features variable stage burn times, booster kick angle, nosecone half-angle, and the pitch programs of both stages (case 6). Fifty control variables are used to discretize the first and second stage pitch program history. In this problem, fifty-four control variables are optimized to obtain the maximum payload capability that satisfies the three equality and three inequality constraints.

All the above problems assume a vehicle of length 160 ft and diameter of 23.33 ft. In case 7, the length and the diameter are also allowed to be optimized. Since this tends to make the vehicle shorter and broader, in case 8, base drag is included, and its effect on the slenderness ratio is studied.

Maximum permissible dynamic pressure tends to become critical since the aerodynamic loading is directly proportional to the dynamic pressure. Assuming a gravity turn for the first-stage (case 5) causes a peak dynamic pressure of $461.49\frac{lb}{ft^2}$, while optimizing the first-stage pitch angle also (case 6) causes a maximum dynamic pressure of $653.83\frac{lb}{ft^2}$. In case 9, dynamic pressure constraints are applied successively to the baseline problem (case 6) of class II. Peak dynamic pressure levels are constrained at 500, 550, and $600\frac{lb}{ft^2}$, and the various cases are compared.

Aerodynamic load is the product of the dynamic pressure and the angle-of-attack in degrees [24]. Large angle-of-attack introduces large lateral loads, which in turn calls for large control requirements. So, lower aerodynamic loads are vital for the structural safety of the vehicle. To ensure that the peak aerodynamic load does not

exceed some pre-fixed value, an aerodynamic load constraint is introduced in case 10.

Discussion of results

The above described ten cases are optimized using SQP. Figure 4 gives a summary of the results discussed below. The shaded region shows the optimized values of the design variables. The payload is the performance index to be maximized.

The baseline problem (case 1) gives a smooth optimized pitch program for the second stage which runs from 50 deg to -30 deg (Figure 4.4). This is reasonable, because, the vehicle starts with an initial flight path angle of 89.7 deg, and is steered into a final flight path angle of zero degrees to satisfy circular orbit conditions. In this case, the kick angle is 0.3 deg. In case 2, when propellant loading is optimized, the performance increases by 24.46%. The pitch angle history does not differ much from that of case 1. In case 3, when the booster kick angle is introduced as a control variable, the first-stage burn time is reduced and the optimized kick-angle is 0.43238°. There is a 21.49% increase in the payload capability over the previous case. The pitch program (Figure 4.4), though in the same range, is appreciably different from that for the baseline problem. This is because, pitch program is the sum of flight-path-angle and angle of attack. Since the booster kick angle is different, the pitch program is different though the trend remains the same.

The above cases assume a constant drag coefficient. In case 4, when the aerodynamic model is introduced, the resulting drag coefficient is smaller than the assumed constant drag coefficient of 0.4, especially in the subsonic region. So, a better performance is obtained. The optimum booster kick angle varies slightly from the previous case. Because of the smaller aerodynamic forces, the first stage burn time is increased

Figure 4.3: Comparison of Optimal Launch Parameters for Various Cases

Case	Stage-1 Burn time (sec)	Stage-2 Burnout time(sec)	Propellant loading	Kick Angle (deg)	C_d	Nosecone Half-angle (deg)	Stage-1 Steer prog	Slenderness ratio	Base Drag	Optimal Payload mass (slug)
1	131.8	238.04	fixed	0.3	0.4	not modeled	gravity turn	0.1458	No	451.29
2	131.0	236.38	variable	0.3	0.4	not modeled	gravity turn	0.1458	No	561.71
3	129.39	237.87	variable	0.43238	0.4	not modeled	gravity turn	0.1458	No	682.46
4	133.96	239.0	variable	0.36706	variable	25.00	gravity turn	0.1458	No	811.15
5	134.43	236.83	variable	0.41541	variable	17.02	gravity turn	0.1458	No	983.69
6	116.15	256.53	variable	13.6115	variable	26.04	variable	0.1458	No	1341.11
7	117.38	258.42	variable	9.26440	variable	29.11	variable	0.2265	No	2137.79
8	116.48	259.42	variable	11.6505	variable	28.48	variable	0.1876	Yes	2097.29

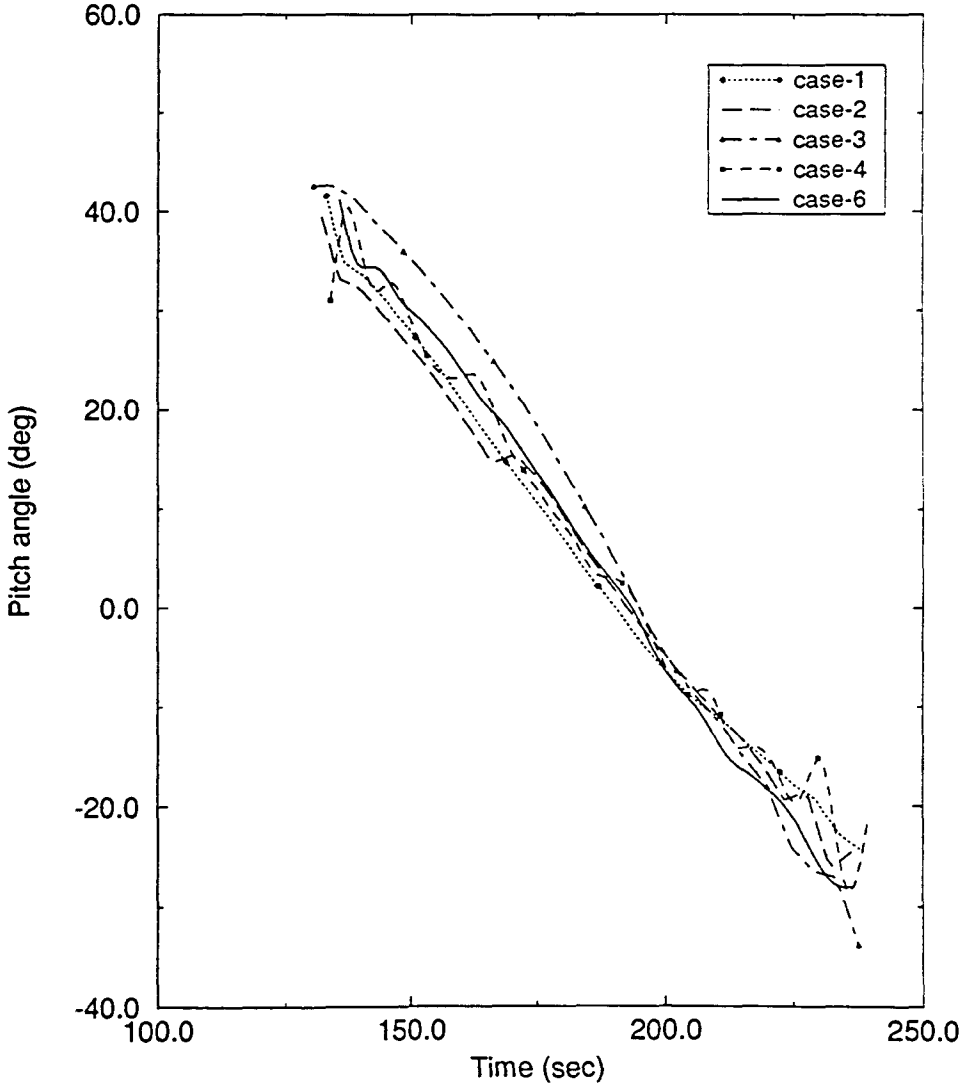

Figure 4.4: Second-Stage Pitch Program for Class I Problems

slightly, but the second stage burn time is reduced, which explains the increased performance. This gives a 18.86% increase in payload over the previous case since the drag is significantly lower, especially in the subsonic region.

Finally, the payload improves by an additional 21.27% when the half-angle of the nosecone is allowed to be optimized (case 5). The stage I burn time for this case does not vary much from the previous case, but the stage II burn-out time is reduced which explains the improved performance (case 4). A smooth pitch program is obtained for this case (Figure 4.4). Since this class of problems assume a gravity turn in the first stage, the aerodynamic forces due to angle-of-attack are zero. Also, pressure drag, which contributes a large quantity to the drag of the vehicle, is directly proportional to the half-angle of the nosecone. So, to minimize the drag, the optimizer reduces the cone half-angle. The cone length is increased such that l_{rem} is zero, which means that the payload is entirely contained in the nosecone. This reduces the structural mass of the payload bay compared to the previous case where l_{rem} is 11 ft.

In class II type problems, when the first-stage pitch angle is allowed to be optimized, the first stage burn time is much smaller than for class I problems. This is due to the higher aerodynamic forces that are associated with non-zero angle-of-attack. The other result typical for this class of problems is that the optimized kick angle is much higher. The optimized kick angle for case 6 is 13.1°, compared to the 0.4154° for case 5, which assumes a gravity turn. The half-angle of the nosecone remains unconstrained but settles at a higher angle. This is because of the aerodynamic normal coefficient due to angle of attack. The payload is improved relative to case 1 by 36.33%.

In case 7, when the optimizer is allowed to choose it own length and diameter

for the vehicle, i.e., its slenderness ratio ($\frac{d}{l}$), there is a remarkable improvement in payload. The payload increases by 59.40%. All the above cases assumed a vehicle of length 160 ft and diameter 23.32 ft. The optimizer chooses a higher slenderness ratio'i.e., the diameter is increased from 23.32 ft to 27.00 ft, while the length of the vehicle is reduced from 160.00 ft to 123.00 ft. This is because propellant loading is optimized. Since propellant mass forms a significant amount of the total mass, the shape of the vehicle is dictated by the propellant. Since the shape for maximum volume subject to a fixed surface area is a sphere, the propellant always tries to assume a near spherical shape. This results in an increased slenderness ratio. The kick angle is also lower in this case.

Next, in case 8, base drag is added to the aerodynamic model to study its effect on the slenderness ratio. Since base drag is directly proportional to the vehicle diameter, the slenderness ratio is decreased by the optimizer. The optimized length and diameter are 140.33 ft and 25.5 ft, respectively. The optimized cone half-angle is 28.48°. Due to the increase in drag, the performance decreases by 1.894%. The optimized kick angle is also higher.

Figures 4.5 gives the velocity histories of all the eight cases discussed above. It is clear that the trends are similar, though the final burn time varies for each case. Figure 4.6 shows the flight path angle history of each case. It can be seen from this figure that the initial kick angle for class I problems (cases 1-5) is small compared to those for the class II problems (cases 6-8). The shorter first-stage burn time for class II problems can also be seen. It is clear that the flight path angle is forced to zero at the final time. The altitude histories of the eight cases are shown in Figure 4.7, and Figure 4.8 shows the optimal trajectories for all the eight cases. It can be seen

that the orbital altitude of 100 nm is reached at the final time. Figure 4.4 shows the optimized second-stage pitch programs for the class I problems. Figure 4.9 gives the optimized pitch programs for both stages for class II problems. Figure 4.10 shows the mass time histories for all eight cases. Figure 4.11 gives the angle-of-attack history for case 6.

The length of the two stages for the above discussed eight cases is given in Table 4.1. It can be seen that in case 4 that when the cone-angle is set fixed, 11.275 ft of the cylindrical portion of the vehicle also forms part of the payload bay. When cone angle is allowed to vary in case 5, the optimizer chooses a lower cone-angle and increases the length so that l_{rem} is zero. By this, the structural mass of the payload bay is reduced. In case 6, when first stage pitch history is also optimized, it is seen that more propellant is loaded in the second stage than the first. This is done to reduce the loss due to the aerodynamic forces that occur in the first stage. In case 7, when the optimizer is allowed to choose its own vehicle length and diameter, it can be seen that a short and broad vehicle is chosen. The reason for this has already been discussed to be due to the tendency of the propellant to assume the optimum shape, which is spherical. In case 8, when base drag is included, the vehicle is made longer and more slender.

In the class II baseline problem, where the pitch programs, nosecone half-angle, kick angle, and propellant loading are optimized, the dynamic pressure level is unconstrained and reaches a maximum of 653.83 $\frac{lb}{ft^2}$. An inequality constraint restricting the maximum permissible dynamic pressure is added to the already existing three equality and three inequality constraints (case 9). This constraint is imposed at the point where the maximum dynamic pressure occurs in the unconstrained case, i.e.,

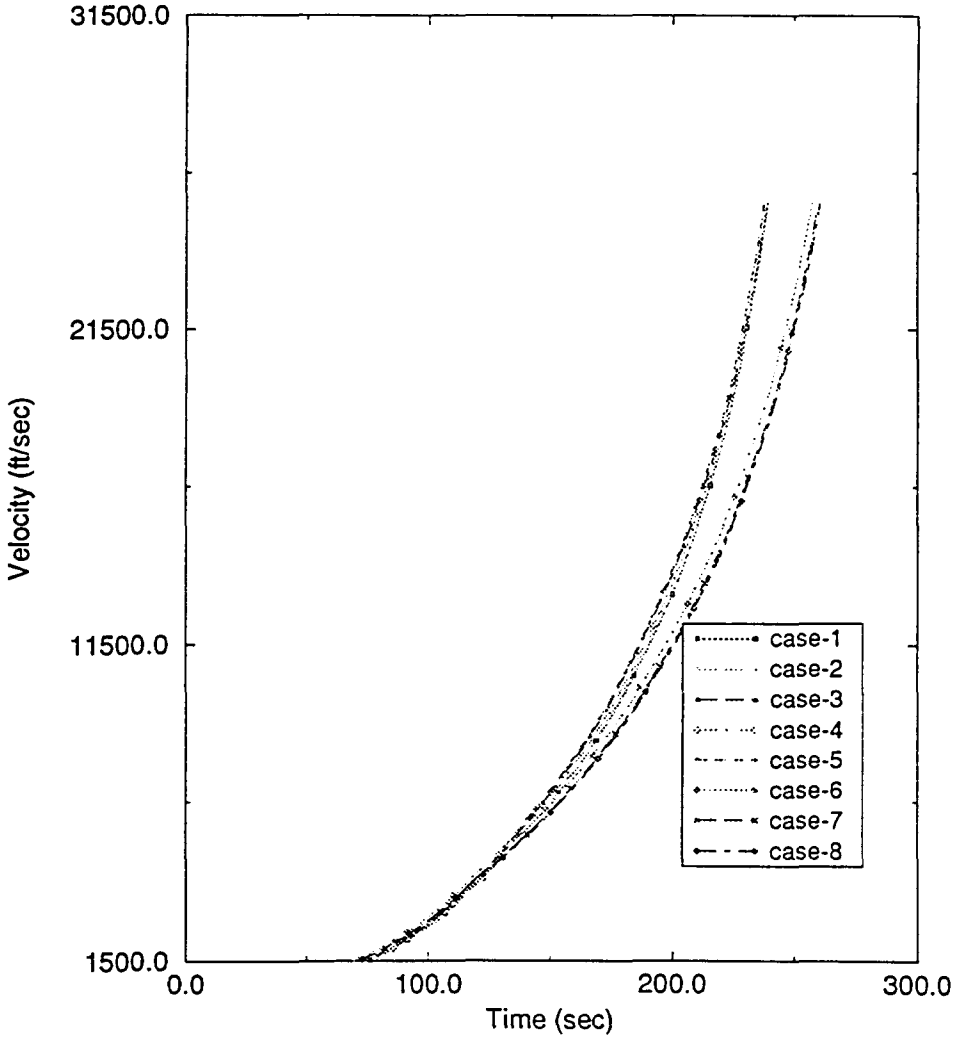

Figure 4.5: Velocity History

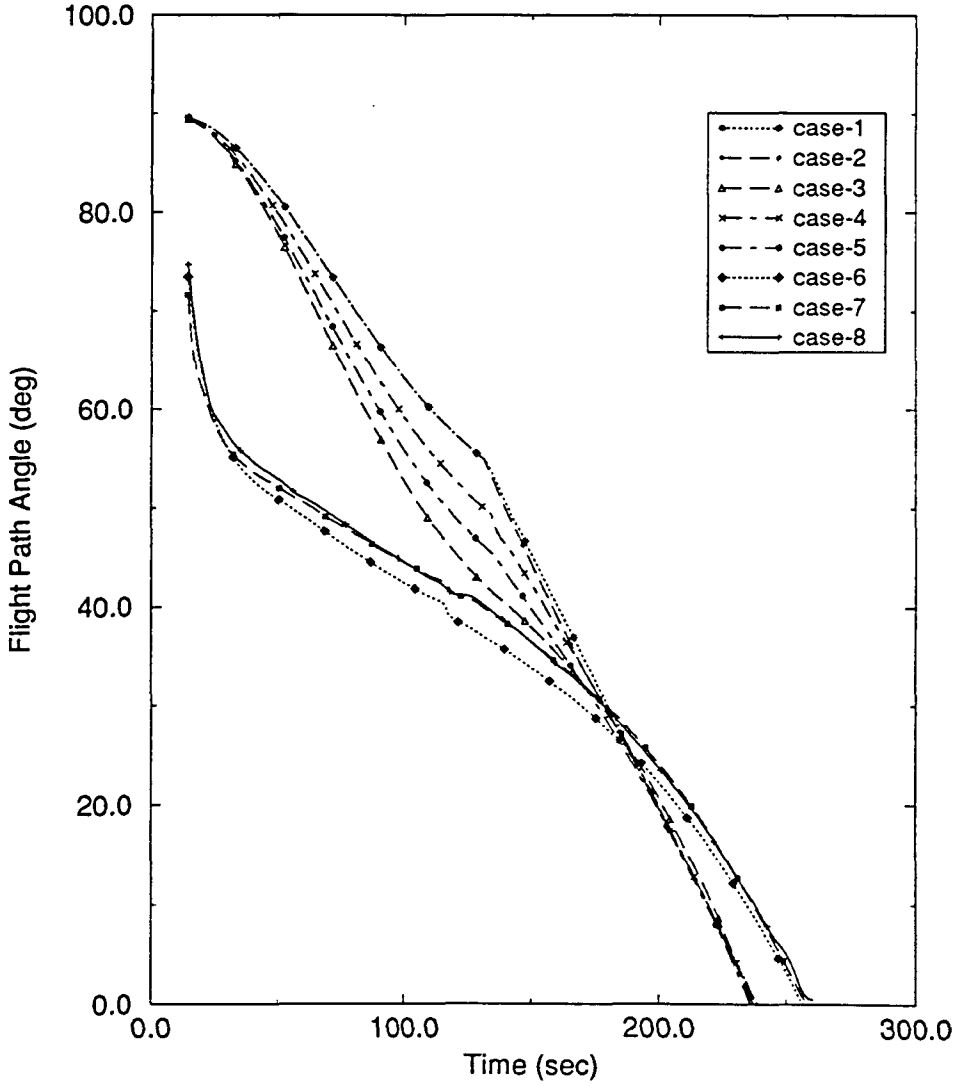

Figure 4.6: Flight Path Angle

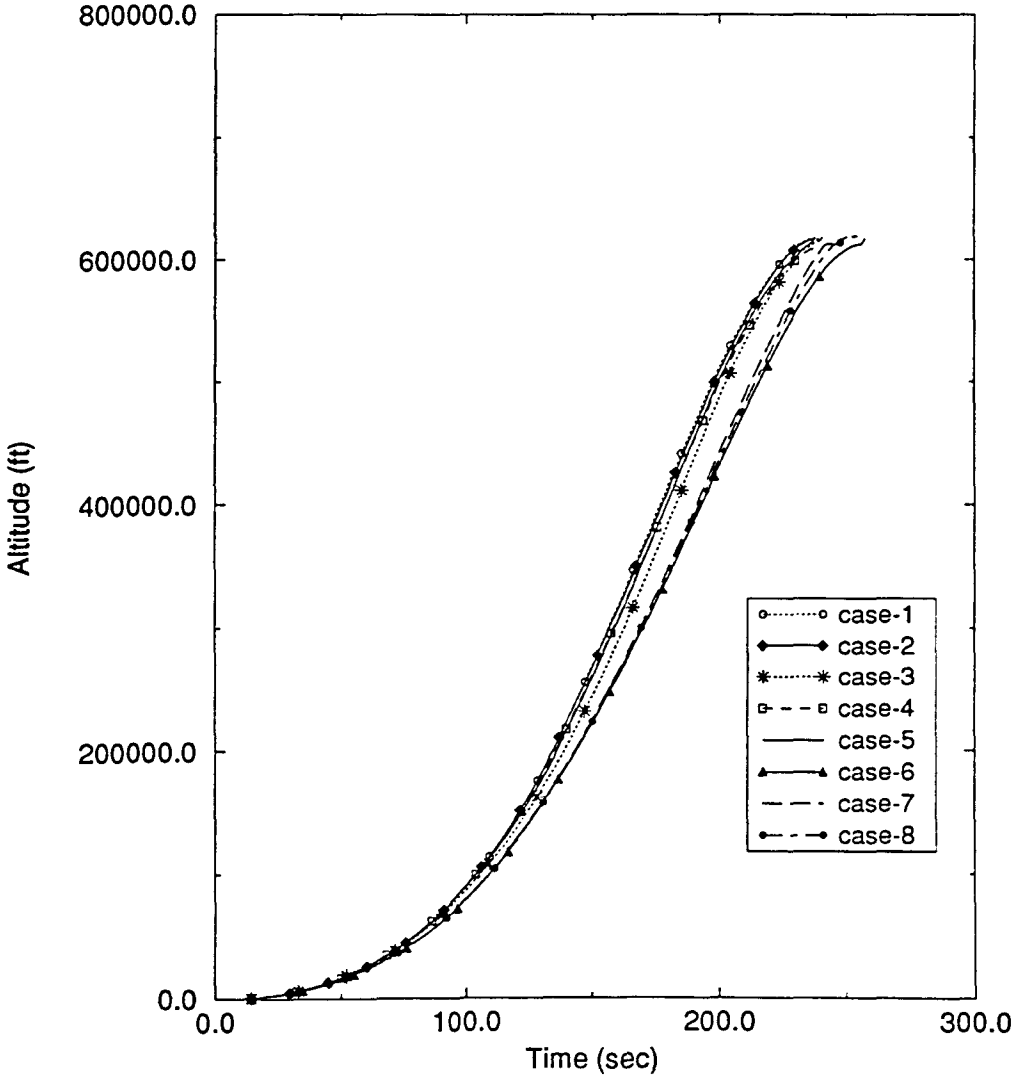

Figure 4.7: Altitude History

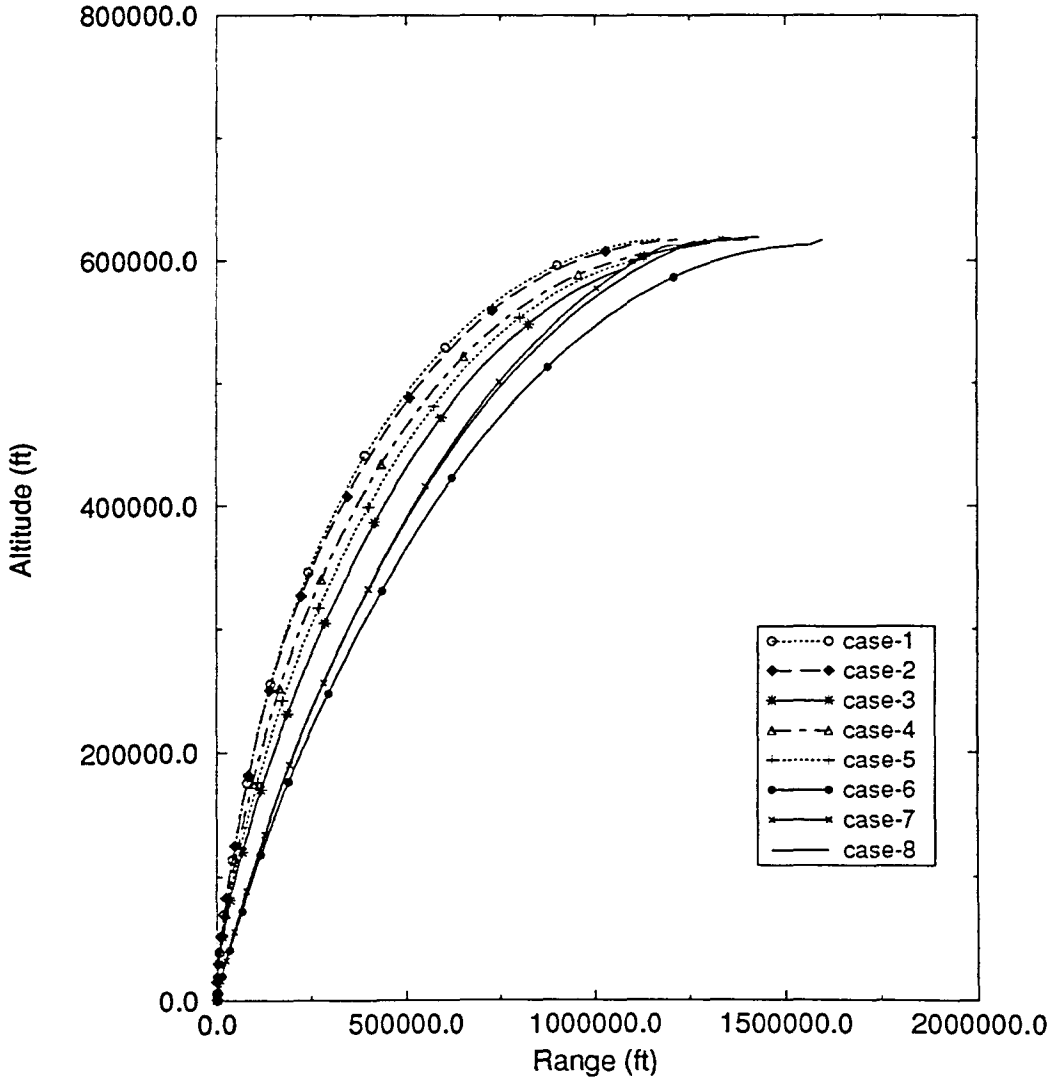

Figure 4.8: Range vs Altitude

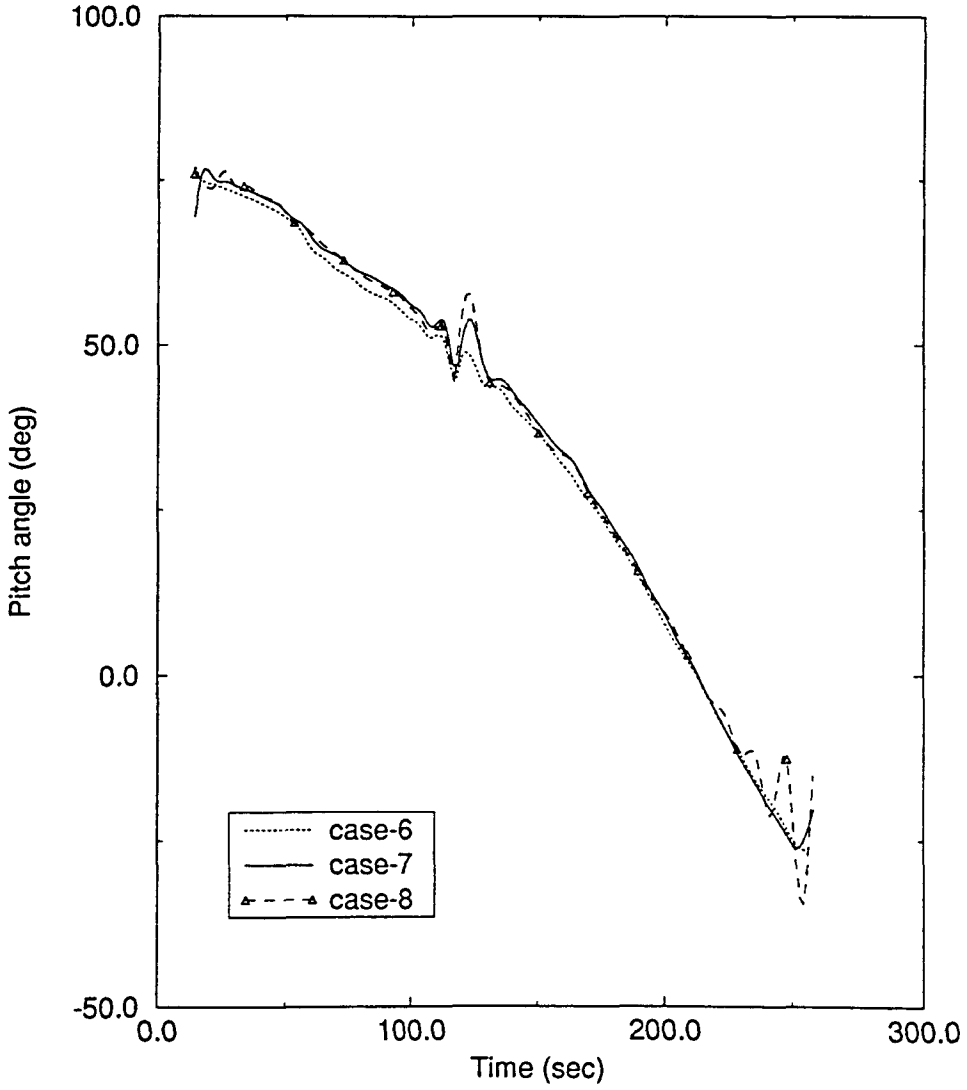

Figure 4.9: Pitch Angle Profile for Class II Problems

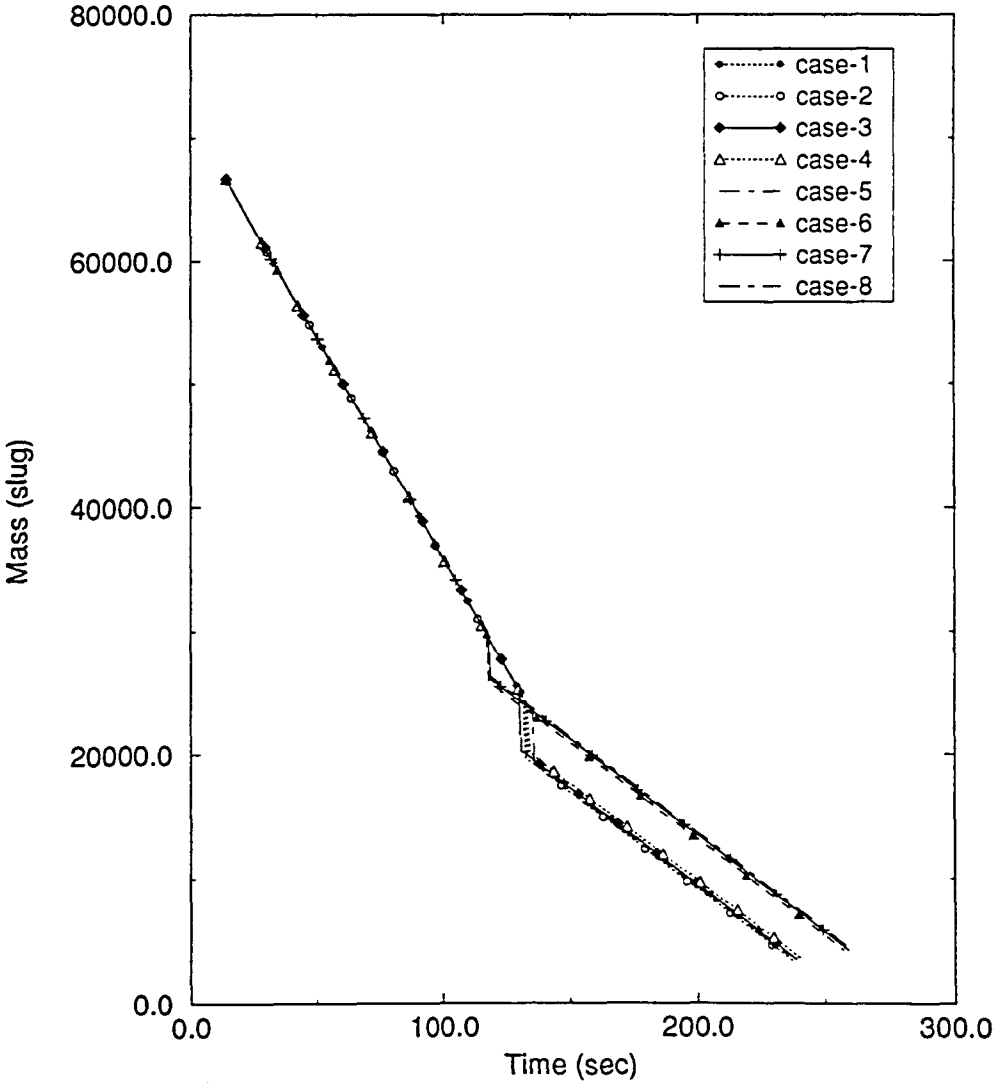

Figure 4.10: Mass History for Class I and Class II Problems

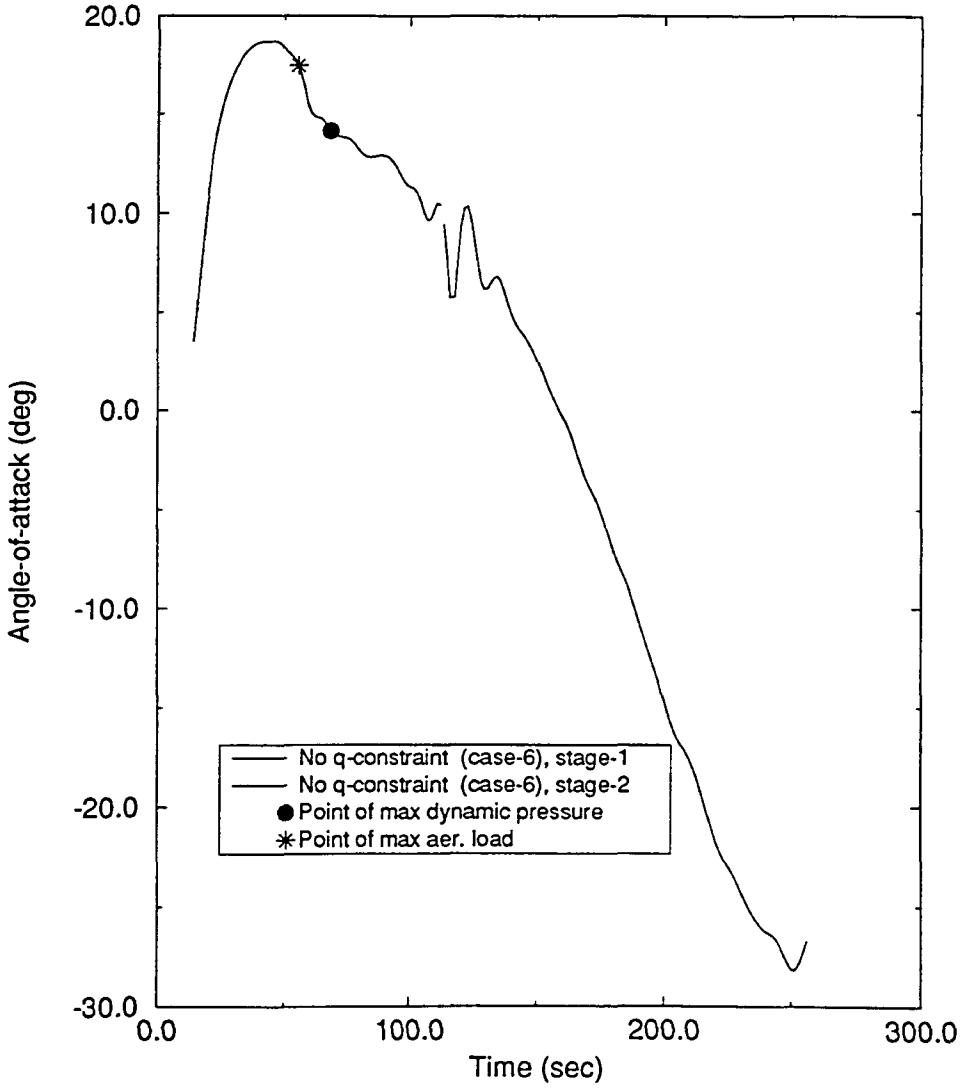

Figure 4.11: Angle-of-attack History for Case 6

Table 4.1: Stage Lengths for the Various Cases

Case	Stage I length ft	Stage II length ft	Nose-cone length ft	l_{rem} ft	Total length ft
1	61.215	67.139	-	-	160.00
2	61.428	66.707	-	-	160.00
3	60.705	68.475	-	-	160.00
4	56.265	67.353	25.107	11.275	160.00
5	57.190	64.575	38.235	0	160.00
6	49.866	85.677	24.525	0	160.00
7	36.248	62.349	25.151	0	123.748
8	43.143	74.647	23.543	0	140.336

in case 6. It is observed that a single inequality constraint applied at the maximum point is sufficient to lower the dynamic pressure level to the constrained limit at all the other points. Figure 4.12 shows how the entire dynamic pressure history is restrained below $550\frac{lb}{ft^2}$, when a single inequality constraint is imposed at the maximum point of the unconstrained case. In cases where a single constraint is not sufficient to restrain the entire history within the constrained level, constraints are applied simultaneously at time points where the maximum permissible level is violated until the constraint is satisfied at all points.

In case 9, when dynamic pressure constraints are applied restricting the maximum dynamic pressure level to various levels, namely, 600, 550, and 500 $\frac{lb}{ft^2}$ respectively, it is observed that the booster kick angle and the half-angle of the nosecone tend to shift towards the gravity turn case values, i.e., as the maximum permissible dynamic pressure level is lowered, the optimal kick angle and nosecone half-angle values become smaller and tend to approach their respective optimal values during the first-stage gravity turn. Figure 4.13 shows the effect of imposing a dynamic pressure constraint on the angle-of attack. Note that the maximum angle-of-attack α is 19

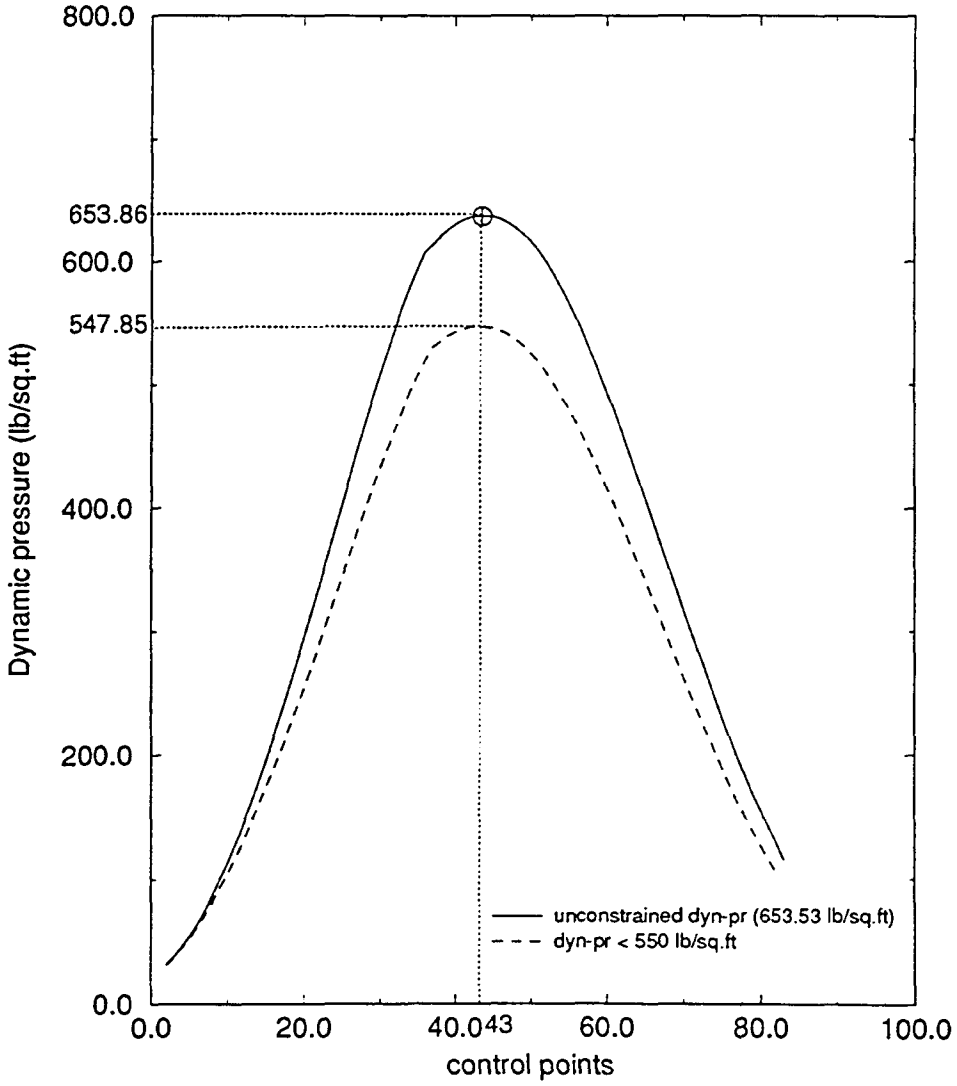

Figure 4.12: Application of Dynamic Pressure Constraints

deg for case 6, where there is no dynamic pressure constraint, while the maximum α reduces to 15 deg when the dynamic pressure is constrained to lie below 600 $\frac{lb}{ft^2}$.

Figure 4.14 gives the velocity profile, when various peak dynamic pressure constraint are imposed. It can be seen that the velocity profile does not vary much. It merely adjusts itself to remain within the constrained dynamic pressure limit. As the permissible dynamic pressure level is lowered, the kick angle is seen to move towards the kick angle for the gravity turn case as shown by Table 1.2. Since the kick angle behaves in such a fashion, the initial flight path angle, which is the complement of the kick angle, also shifts towards the gravity turn case (Figure 4.15). Table 4.2 gives the optimized booster kick angle and nosecone half-angle and shows this trend when dynamic pressure constraints are imposed.

Table 4.2: Effects of Imposing Dynamic Pressure Constraints

Maximum Dynamic Pressure lb/sq.ft	Cone Angle deg	Kick Angle deg	Payload Mass slug
No constraints(653.86)	26.04	13.612	1341.11
600	25.79	12.439	1323.03
550	25.61	8.5229	1314.96
500	25.20	7.0549	1239.83
Gravity turn(461.49)	17.02	0.4154	983.69

The variation of the dynamic pressure profile with maximum dynamic pressure constraint is shown in Figure 4.16. Figures 4.17 and 4.18 show the pitch program and the aerodynamic heating parameter variation with various levels of dynamic pressure constraints. The pitch program behaves similar to the flight path angle in the first stage. Since, the aerodynamic heating parameter is the product of the dynamic pressure and the velocity cubed ($\frac{\rho v^3}{2}$) [24], the heating parameter variation is similar

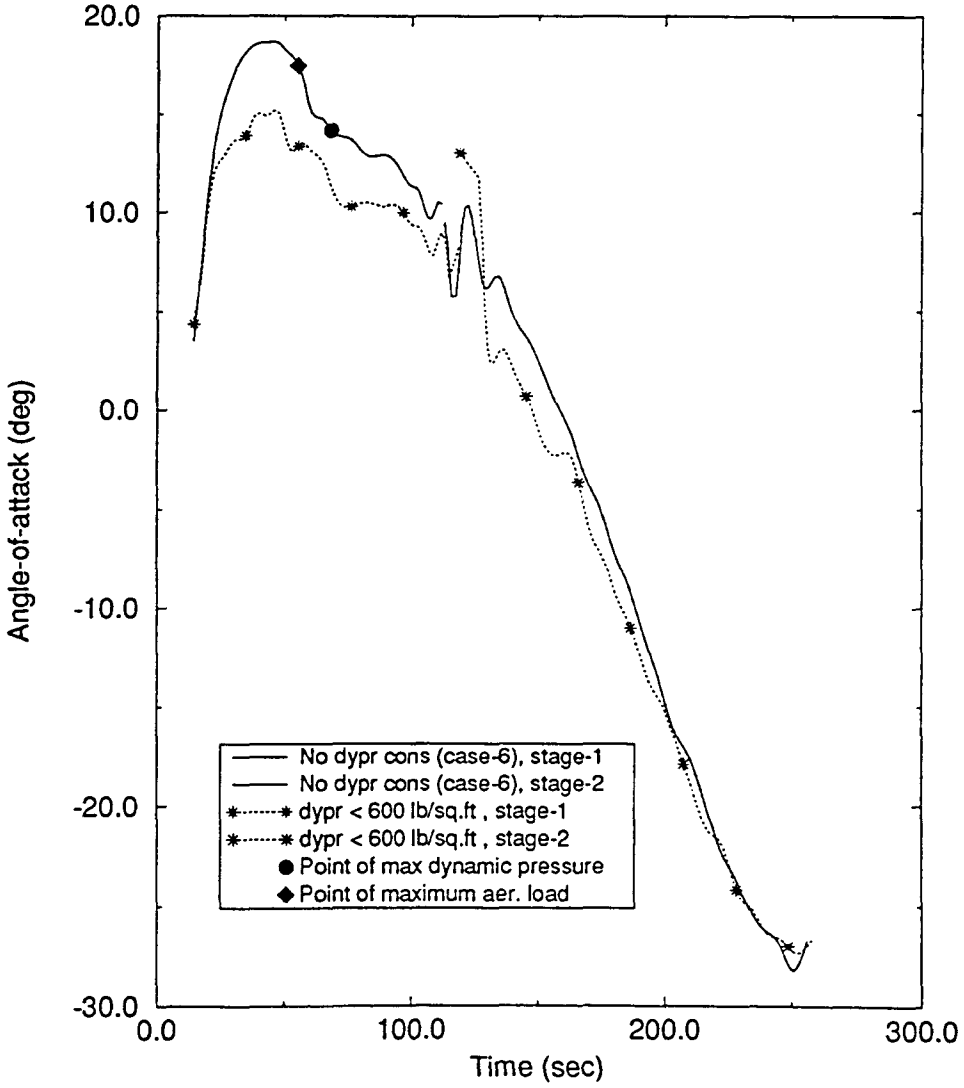

Figure 4.13: Effect of Dynamic Pressure Constraint on Angle-of Attack History

to the dynamic pressure variation.

First-stage gravity turn is used to reduce the lateral structural loads on the vehicle. When the first-stage pitch program is allowed to be optimized, large angles of attack of the order of 19 deg occur (Figure 4.11). To ensure that the peak aerodynamic load does not exceed some pre-fixed value, an aerodynamic load constraint is introduced in case 10. Figure 4.19 shows the aerodynamic load profile when the peak load value is constrained to within 8600 lb deg/ft^2. A single constraint applied at the point where maximum aerodynamic load occurs in the unconstrained case is sufficient to constrain the entire load history within this value. The reaction of the angle-of-attack history to this load constraint can be seen in Figure 4.20. It is obvious that constraining the maximum aerodynamic load lowers the peak angle-of-attack in the first stage. The effect of this constraint on dynamic pressure is shown in Figure 4.21. This figure also shows the dynamic pressure history when the maximum dynamic pressure is constrained.

An interesting observation is that, both first and second stage burn times have to be simultaneously optimized to obtain smooth pitch program histories. During the initial phase of the research, only the second stage burn time was optimized, and in most cases, this ended up in a highly oscillatory type of pitch profile. This was due to the excess energy available. This effect was proportional to the fixed mass removed at the end of the first stage. The oscillations increased in amplitude as more mass was removed at the end of the first stage because the vehicle became lighter and more energy was available. But when the first stage burn time was also included in the optimization, the oscillations in the pitch program history disappeared. The optimizer varied the first stage burn time to give a smooth pitch program profile.

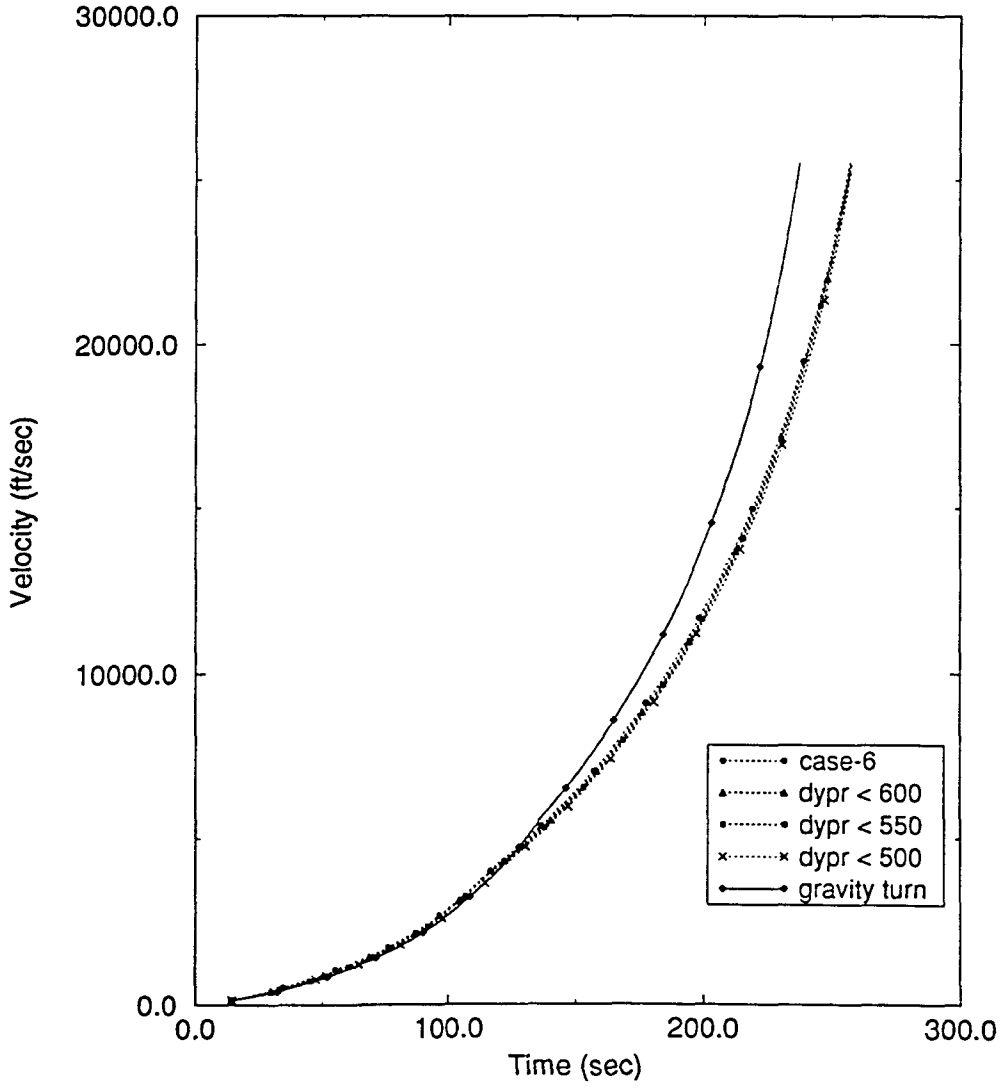

Figure 4.14: Velocity Profile Variation With Dynamic Pressure Constraint Levels

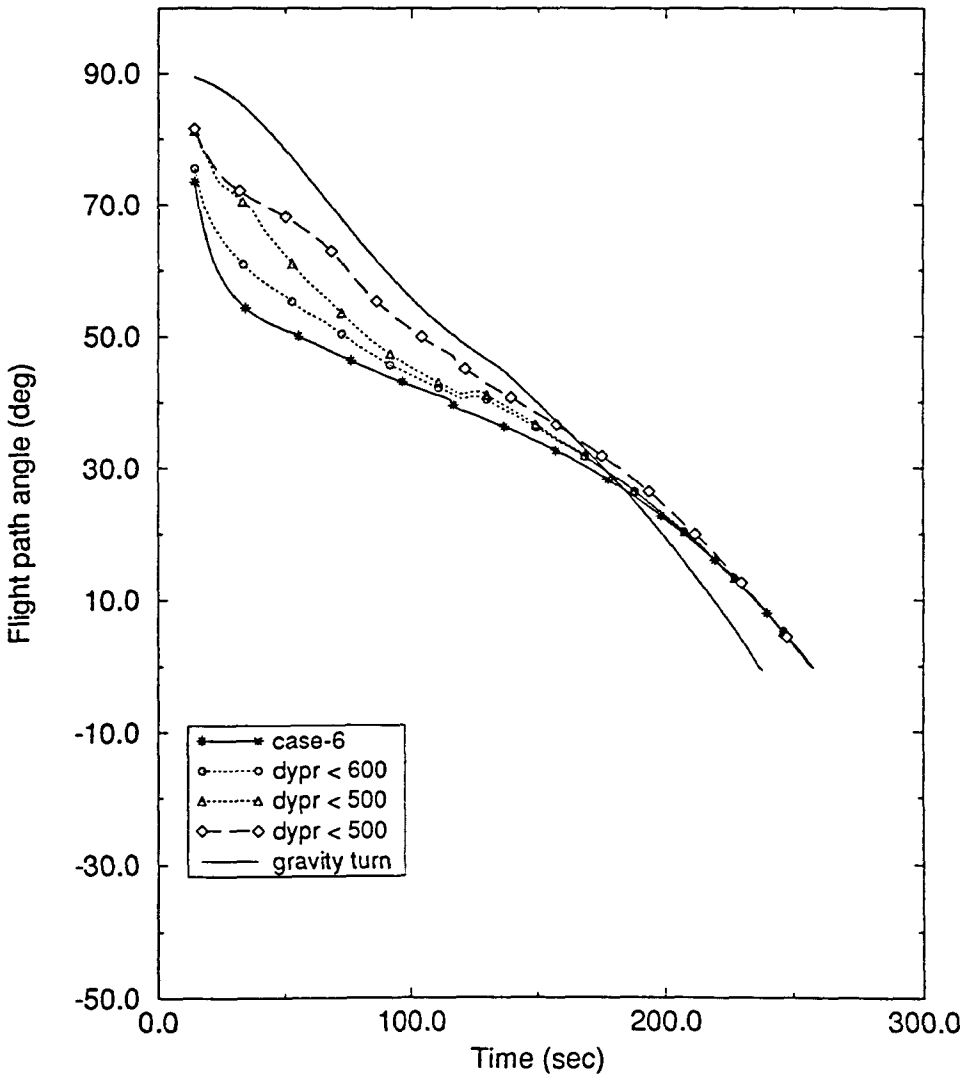

Figure 4.15: Flight Path Angle Time History Variation With Dynamic Pressure Constraint Levels

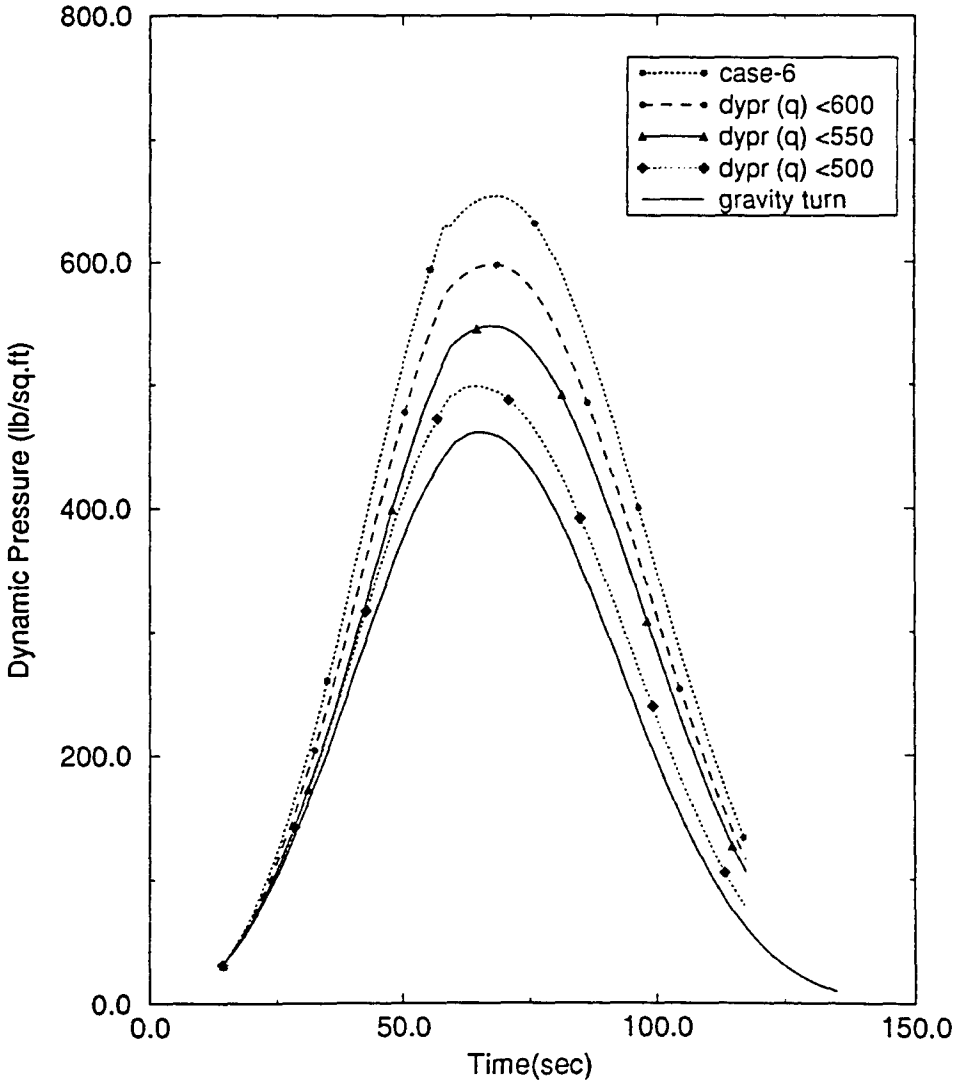

Figure 4.16: Comparison of Dynamic Pressure Histories

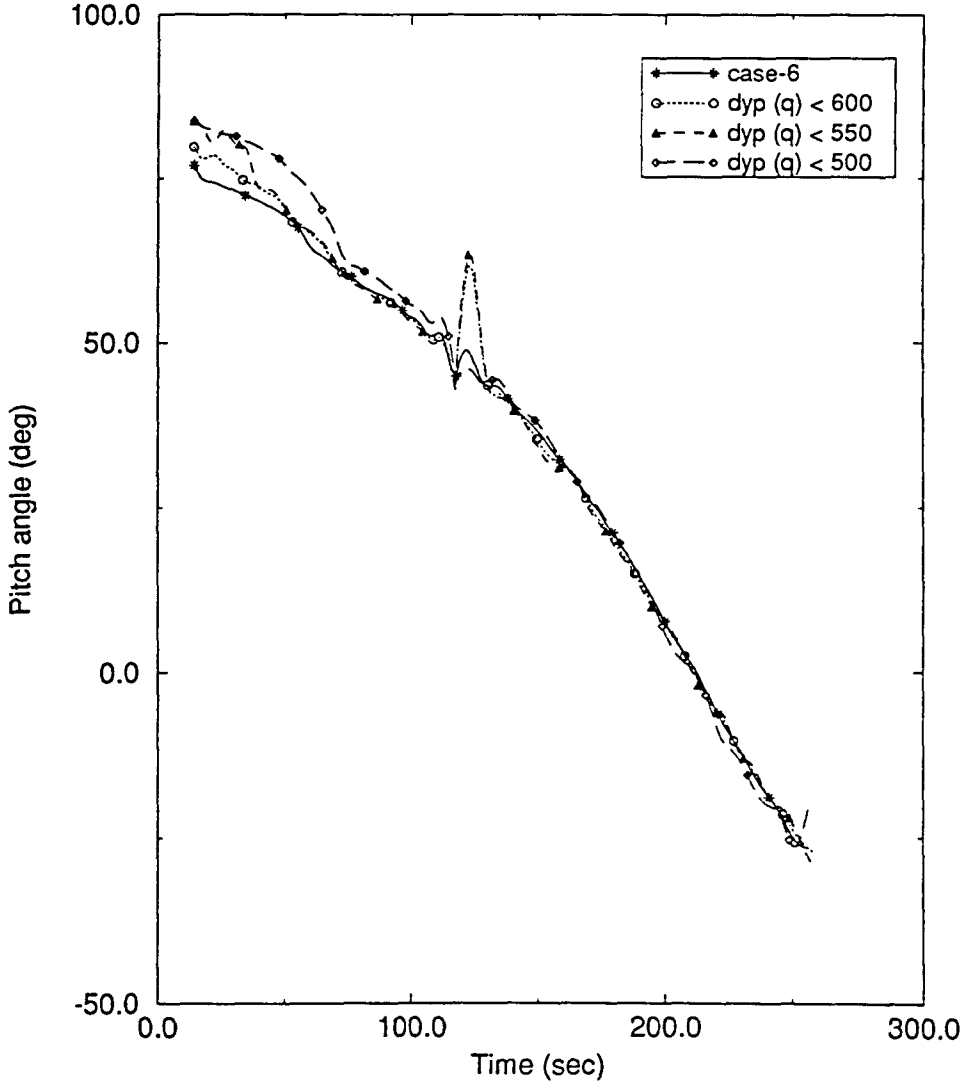

Figure 4.17: Pitch Program Variation With Dynamic Pressure Constraints Levels

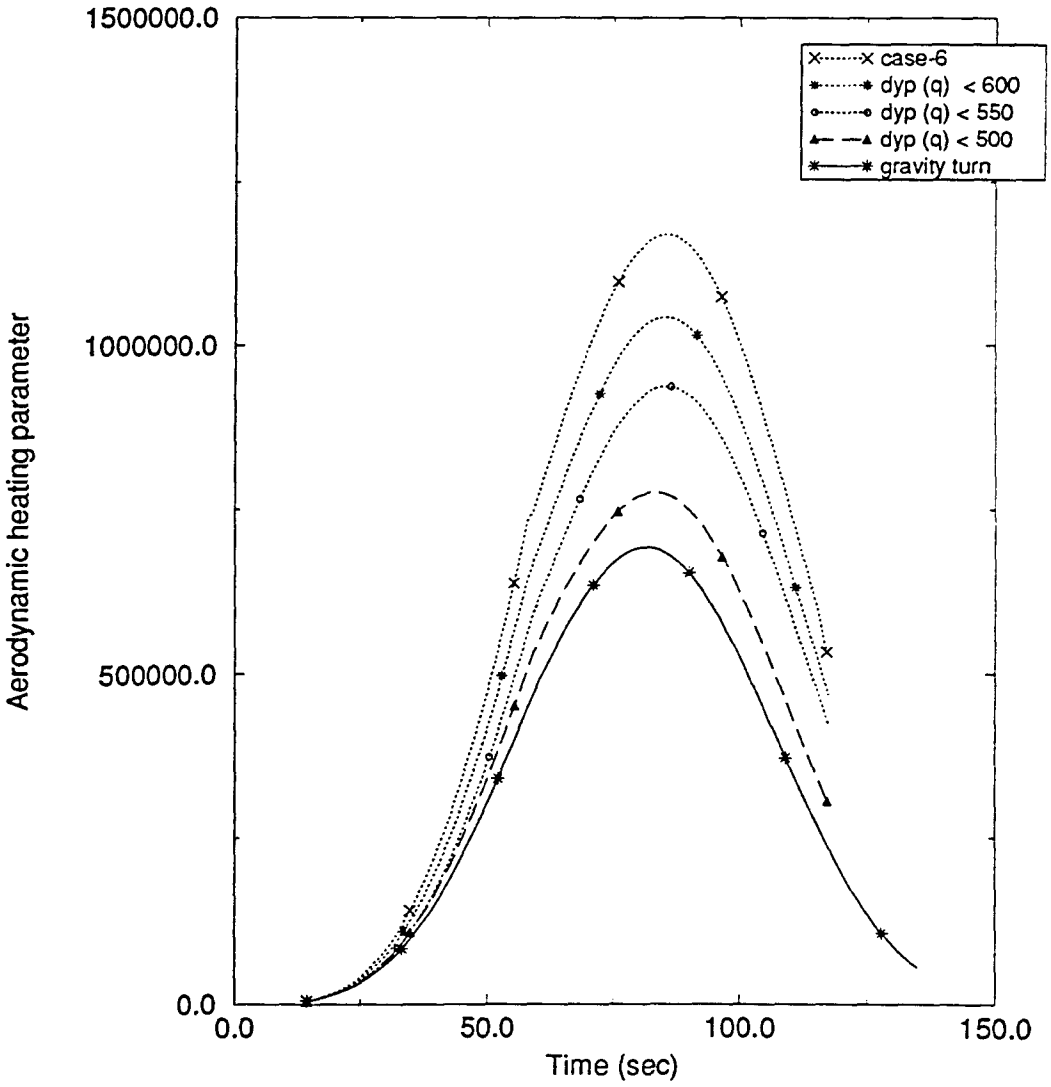

Figure 4.18: Aerodynamic Heating Parameter History Variation With Dynamic Pressure Constraint Levels

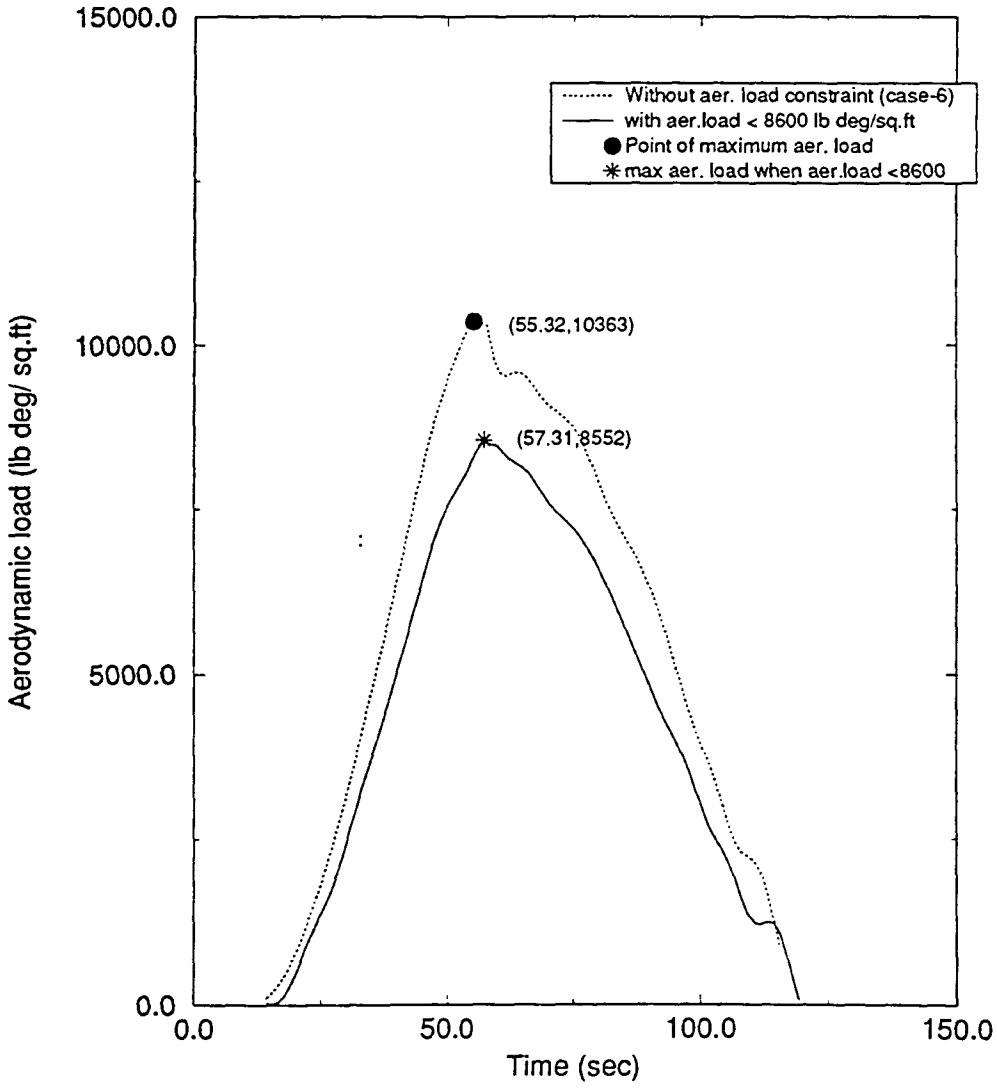

Figure 4.19: Aerodynamic Load Constraints

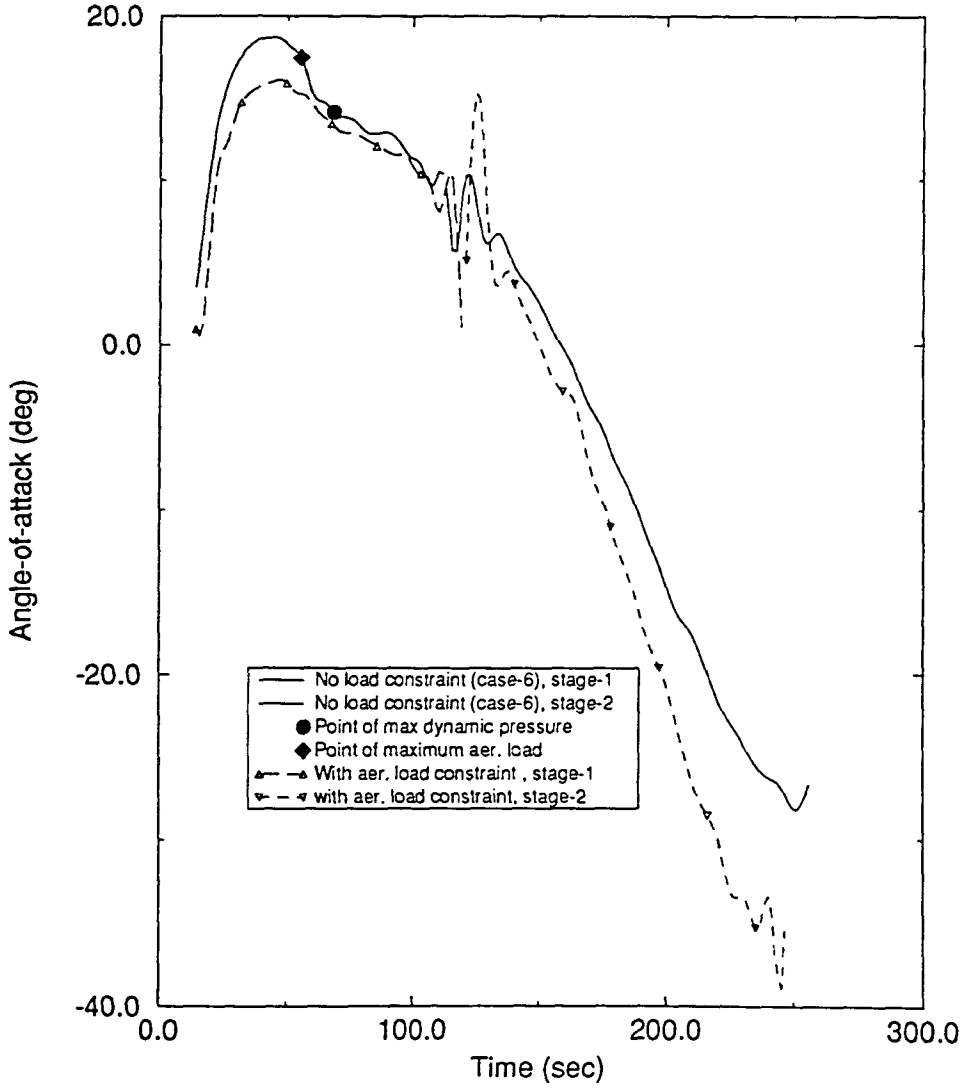

Figure 4.20: Effect of Aerodynamic Load Constraints on Angle-of-Attack

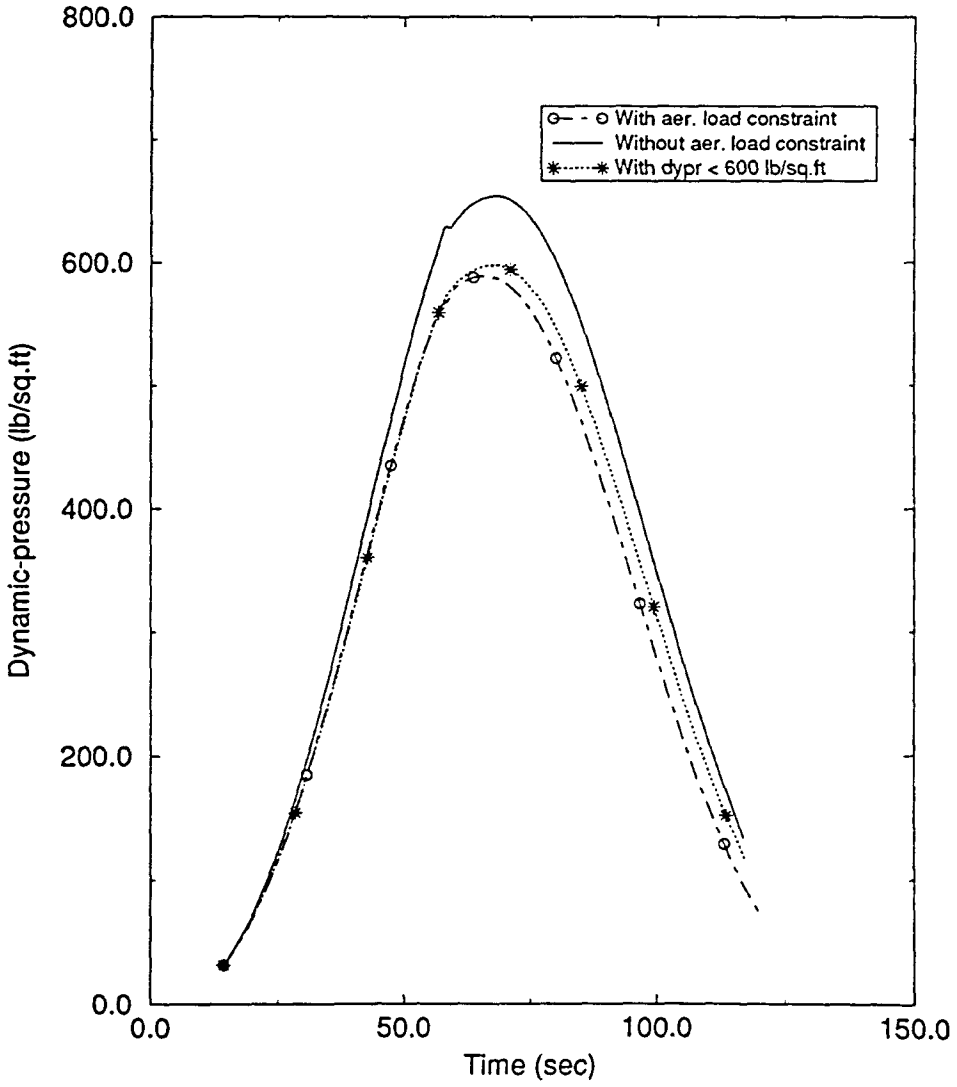

Figure 4.21: Effect of Dynamic pressure and Aerodynamic Load Constraints on Dynamic Pressure

CHAPTER 5. CONCLUSIONS AND RECOMMENDATIONS

Conclusions

From the discussions in chapter 4, it can be concluded that an improvement of 56.38% in payload can be obtained by optimizing the design variables along with the trajectory variables. In this study, very few design parameters such as nosecone angle, slenderness ratio, propellant loading have been considered. Of these, the slenderness ratio is seen to have a very large impact on the payload. The next significant parameter is the kick-angle. It has been observed that kick-angle is a very sensitive input control variable.

The most sensitive trajectory parameter is the booster kick angle. Proper selection of the guess value is essential for convergence. The next important parameter is the nosecone half-angle. The shape of the nosecone is generally selected on the basis of combined aerodynamic, and structural considerations. For example, a hemispherical nose has a very high drag from the performance standpoint, but it is excellent from the standpoint of structural integrity. Since the pressure drag may be several times that due to friction at supersonic speeds, careful selection of the nose shape is important to assure satisfactory performance and operation of the over-all system. A very simplified method has been adopted to calculate the structural weight. It can be seen that class II problems give better performance than class I problems. The

first-stage of class II problems burn-out earlier than class I problems. The optimal kick-angle of class II problems are higher than class I problems.

When dynamic pressure constraints are applied on class II problems, an interesting phenomenon is observed. The optimal nosecone angle and kick-angle move towards the corresponding values of class I problems as constraint level is decreased.

A peak angle-of-attack of 19 deg occurs when the first-stage pitch program is allowed to be optimized. Aerodynamic load constraints can be applied to reduce the peak angle-of-attack. A single constraint applied at the peak point of the unconstrained case is sufficient to constrain the entire trajectory.

Base-drag is a very important factor when slenderness ratio is optimized. Optimizing propellant loading tends to increase the slenderness ratio of the vehicle, while taking into account base-drag effects decreases the slenderness ratio. In other words, neglecting base-drag results in a shorter and broader vehicle, while including base-drag results in a longer and more slender vehicle.

Recommendations

Aerodynamic and structural modeling are separate subjects that require in-depth study and massive computational resources. Due to the large number of design variables and time constraints, many assumptions and approximations were made. The following recommendations are made for further study:

- The present study assumes a 0.5 inch thick solid aluminum cone-cylinder shell for the structure. In reality, the outer casing is made of skin stiffened by stiffeners. A more realistic structural modeling can be used to obtain the structural masses.

- Direct structural integrity constraints such as critical load for column bucking and bending can be introduced.
- A more sophisticated aerodynamic model can be used with a three-dimensional rotating earth model.
- The structural weight and its dependence on propellant loading can be more appropriately modeled.
- A more complex vehicle configuration can be assumed.

Such a detailed study will make an excellent multi-disciplinary design problem. But a large amount of computational resources and time will be needed.

REFERENCES

[1] Malina, J.F., and Summerfield, M., "The Problem of Escape from the Earth by Rocket," *Journal of the Aeronautical Sciences* Vol.14, No.8, 1947, pp.471-480.

[2] Goldsmith, M., "On the Optimization of Two-Stage Rockets," *Jet Propulsion* Vol.27, No.4, 1957, pp.415-416.

[3] Hall, H.H., and Zambelli, E.D., "On the Optimization of Multistage Rockets," *Jet Propulsion* Vol.28, No.7, 1958, pp.463,465.

[4] Coleman, J.J., "Optimum Stage-Weight Distribution of Multistage Rockets," *ARS Journal* Vol.31, No.2, 1961, pp.259-261.

[5] Srivastava, T.N., "Optimum Stage Weight Distribution of Multistage Rockets," *ARS Journal* 1962, Feb.

[6] MacKay, J.S., Rossa, L.G., and Leonard, G., "A Variational Method for the Optmization of Interplanetary Round-Trip Trajectories," NASA TN D-1660, 1963.

[7] Kelley, H.J., Uzzell, B.R., and Mckay, S.S., "Rocket Trajectory Optimization by Second-order Numerical Technique," *AIAA Journal* Vol.7, No.5, 1969, pp.879-884.

[8] Stancil ,R.T., and Kulakowski, L.J., "Rocket Boost Vehicle Mission Optimizations," *ARS Journal* Vol.31, No.7, 1961, pp.935-942.

[9] Jurovics, S., "Optimum Steering Program for the entry of a Multistage Vehicle into a Circular Orbit," *ARS Journal* Vol.31, No.4, 1961, pp.518-522.

[10] Tren, F., and Spurlock, O.F., "Payload Optimization of Multistage Launch Vehicles," NASA TN D-3191, 1966.

[11] Ruppe, H.O.,"Design Considerations for Future Space Launchers," *Acta Astronautica* Vol.29, No.9, 1993, pp.705-722.

[12] Wetzel, T. A., and Moerder, D. D., "Vehicle/Trajectory Optimization for Aerocapture at Mars," *Journal of the Astronautical Sciences* Vol.42, No.1, 1994, pp.71-89.

[13] Kluever, C. A., and Pierson, B. L., "Vehicle-and-Trajectory Optimization of Nuclear Electric Spacecraft for Lunar Missions," *Journal of Spacecraft and Rockets* Vol.32, No.1, 1995, pp.126-132.

[14] Munk, M.M., "The Aerodynamic Forces on Airship Hulls," NACA Report 184, 1923.

[15] Spreiter, J.R., and Alksne, A.Y., "Slender-body Theory Based on Approximate Solution of the Transonic Flow Equation," NASA TR R-2, 1959.

[16] Dyke, V., and Milton, D., "Practical Calculation of Second-order Supersonic Flow Past Nonlifting Bodies of Revolution," NACA TN-2744, 1952.

[17] Shapiro, A.H., *The Dynamics and Thermodynamics of Compressible Fluid Flow,* Ronald Press, London, 1953.

[18] Syvertson, C.A., and Dennis, D.H., "A Second-order Shock Expansion Method Applicable to Bodies of Revolution Near Zero Lift," NACA Report 1328, 1957.

[19] Hamner, R.L. and Leff, A.D., "Linear Aerodynamic Loads on Cone-Cylinders at Mach Numbers from 0.7 to 2.0," NASA CR-413, March. 1966.

[20] Thompson, J.F., "Aerodynamic Characteristics for Cone-Cylinder-Frustum-Cylinder Configurations at Mach numbers from 0.7 to 1.96," NASA CR-737, April. 1967

[21] Perkins, E.W., and Kuehn, D.M., "Comparison of the Experimental and Theoretical Distributions of Lift on a Slender Inclined Body of Revolution at M=2.0," NACA TN-3715, May. 1956.

[22] Chin, S. S., *Missile Configuration Design,* McGraw-Hill, New York, 1961.

[23] Cornelisse, J.W., Schoyer, H.F.R., and Wakker, K.F., *Rocket Propulsion and Spaceflight Dynamics,* Pitman, California, 1979.

[24] White, J.F., *Flight Performance Handbook for Powered Flight Operations,* Wiley, New York, 1963.

[25] Griffin, M.D., and French, J.R., *Space Vehicle Design,* AIAA Education Seri es, 1991.

[26] Whitcomb, R.T, "A Study of the Zero-lift Drag-rise Characteristics of Wing-body Combinations Near the Speed of Sound," NASA RM L52H08, Sept. 1952.

[27] Bryson, A. E., Jr. and Hoffman W. C. "A Study of Techniques for Real-Time On-li ne Flight Path Control-Minimum Time Turns to a Specified Tracks." *Rept. ASI-TR-4,* Sept. 1971.

[28] Bilstein, E. R.,*Stages to Saturn,* NASA SP-4206, June. 1979.

[29] MacKay, J.S., and Weber, R.J., "Performance Charts for Multistage Rocket Boosters," NASA TN D-582, 1961.

[30] *Jane's all the world's aircraft," 1971-72, pp110.*

APPENDIX A. EARTH'S ROTATION

At first-stage burn-out, the increment in velocity due to earth's rotational effects is vectorially added to the burnout velocity vector to account for the earth's rotation. For a 110-degree launch from AMR, the component of velocity, v_{rot}, is 1262 ft/sec [24]. The inertial burnout velocity v_{BOI}, is given by:

$$v_{BOI} = \sqrt{v_{BO}{}^2 + v_{rot}{}^2 + 2v_{BO}v_{rot}sin\beta_{BO}} \tag{A.1}$$

When the earth's rotation is taken into consideration in case 7, the payload is increased as shown below. Similar improvements can be expected for the other

Table A.1: Comparison with and without earth rotation

Case	Payload slug
With rotating earth	1601.66
Without rotation	1341.11

cases as well.

APPENDIX B. VERTICAL RISE SEGMENT

The launch vehicle is assumed to lift-off vertically for 13 sec and then to start pitching. This is done for two reasons. The physical reason is for the vehicle to clear the launch pad. The mathematical reason is to avoid the singularity that occurs in the equation of motion 2.1 at lift-off, when v=0. The following equations are integrated to calculate the state variables at the end of the vertical rise after 13 sec.

$$\frac{dv}{dt} = \frac{T-D}{m} - g \tag{B.1}$$

$$\frac{dh}{dt} = v \tag{B.2}$$

A constant drag coefficient of 0.4 is assumed for the calculations. The state variables at t=13 sec are found to be v=149.89 ft/sec, $\gamma = 90°$, s=0 and h=886.09 ft. These values are used as the initial values for the optimization problems.

APPENDIX C. VEHICLE DEFINITION

The vehicle chosen for this study is a hypothetical two-stage, liquid propellant launch vehicle as presented by White [24]. The launch is assumed to take place at the Atlantic Missile Range with a launch azimuth of 110 deg. The vehicle lift-off weight is 2,309,000 lb. The thrust-to-weight ratio at lift-off is 1.3. The vehicle is assumed to lift-off vertically for 13 sec and then pitch over. The following table gives the input values used.

Table C.1: Launch Vehicle Propulsion and Weight Data

Parameter	Stage I	Stage II
Thrust, lb	3,001,700	2,125,434.5
Specific Impulse, sec	259.885	425
Propellant Sensitive fraction	0.03	0.02
Drag reference area, sq.ft	452	

APPENDIX D. BASE DRAG COMPARISON

The following table shows the decrease in performance when base-drag is included in the aerodynamic model of case 6. It can be seen that the payload capability is reduced by 0.93%.

Table D.1: Comparison with and without base-drag

Case	Payload slug
With base-drag	1328.66
Without base-drag	1341.11

APPENDIX E. PROPELLANT CHARACTERISTICS

Stage I

It is assumed that stage I oxidizer and fuel are liquid oxygen and RP-1 in the weight ratio 2.2:1. RP-1 is a specially refined petroleum product particularly suitable as rocket fuel. The weight densities of liquid oxygen and RP-1 are 71.38 lb/ft^3 and 50.45 lb/ft^3, respectively. Hence,

$$m_{propl} = 2.2m_1 + m_1 \tag{E.1}$$

so that

$$m_1 = \frac{m_{propl}}{3.2} \tag{E.2}$$

Hence, for a cylinder,

$$vol_1 = \frac{2.2m_1 32.2}{71.38} + \frac{m_1 32.2}{50.48} \tag{E.3}$$

Finally, since

$$vol_1 = \pi r^2 l_1 \tag{E.4}$$

$$l_1 = \frac{vol_1}{\pi r^2} \tag{E.5}$$

l_1 gives the stage length required to load the propellant.

Stage II

Stage II is assumed to be loaded with liquid oxygen and liquid hydrogen in the weight

ratio 5:1. The weight density of liquid hydrogen is 4.42 lb/ft^3. So, we have

$$m_{prop2} = 5m_2 + m_2 \tag{E.6}$$

so that,

$$m_2 = \frac{m_{prop1}}{6} \tag{E.7}$$

Hence,

$$vol_2 = \frac{5m_2 32.2}{71.38} + \frac{m_2 32.2}{4.42} \tag{E.8}$$

and

$$vol_2 = \pi r^2 l_2 \tag{E.9}$$

$$l_2 = \frac{vol_2}{\pi r^2} \tag{E.10}$$

APPENDIX F. ENGINE CHARACTERISTICS

The assumed launch vehicle can be classified along with the Saturn-IB series [28]. Based on the thrust and specific impulse requirements, stage I is fitted with two Rocketdyne H-1 engines and stage II with nine Rocketdyne J-2 engines. Given below are the propulsion and weight characteristics of these engines [30].

Rocketdyne H-1 engine

Thrust = 1522000 lb

I_{sp} = 260sec

Dry weight = 18,415 lb

So, the engine weight of two such engines is 36830 lb and $m_{engine1}$ = 1142 slugs.

Rocketdyne J-2 engine

Thrust = 230,000 lb

I_{sp} = 428 sec

Dry weight = 3,480 lb

The engine weight of nine such engines is 31320 lb, and $m_{engine2}$ = 972 slugs..

APPENDIX G. NUMERICAL INTEGRATION SCHEME

The fifth-order Runge-Kutta method by Butcher is used to integrate the equations of motion. If each scalar equation is of the form, $\frac{dy}{dt} = f(t,y)$, then

$$y = y_0 + \frac{1}{90}(7k_1 + 32k_3 + 12k_4 + 32k_5 + 7k_6) \tag{G.1}$$

where

$$k_1 = hf(t,y) \tag{G.2}$$

$$k_2 = hf(t + \frac{h}{4}, y + \frac{k_1}{4}) \tag{G.3}$$

$$k_3 = hf(t + \frac{h}{4}, y + \frac{k_1}{8} + \frac{k_2}{8}) \tag{G.4}$$

$$k_4 = hf(t + \frac{h}{2}, y - \frac{k_2}{2} + k_3) \tag{G.5}$$

$$k_5 = hf(t + \frac{3}{4}h, y + \frac{3}{16}k_1 + \frac{9}{16}k_4) \tag{G.6}$$

$$k_6 = hf(t + h, y - \frac{3}{7}k_1 + \frac{2}{7}k_2 + \frac{12}{7}k_3 - \frac{12}{7}k_4 + \frac{8}{7}k_5) \tag{G.7}$$

where h is the integration step size and $y = y(t_0 + h)$ and $y_0 = y(t_0)$. This method is used since the subroutine was validated and used for previous trajectory studies. A fixed step-size of 0.005 is used to integrate the equations in the normalized time interval of $(\frac{t_0}{t_f}, 1)$.

From time $\frac{t_0}{t_f}$ to the time nearest to $\frac{t_1}{t_f}$, a step-size of 0.005 is used. Then the remaining small time interval is integrated in one step so that the first-stage dynamics

are computed correctly up to time $\frac{t_1}{t_f}$. The second-stage dynamics are also integrated in a similar manner.

The step-size of 0.05 was chosen after test studies with different step-sizes. It was found to be a reasonable compromise between accuracy and computer run-time.